Quarterly Journal of the
Royal Meteorological Society ⬛ RMetS

# Characterising the shape, size, and orientation of cloud-feeding coherent boundary-layer structures

**Leif Denby[1]** | **Steven J. Böing[1]** | **Douglas J. Parker[1]** | **Andrew N. Ross[1]** | **Steven M. Tobias[2]**

[1]School of Earth and Environment, University of Leeds, Leeds, UK

[2]School of Mathematics, University of Leeds, Leeds, UK

**Correspondence**
L. Denby, Institute for Climate and Atmospheric Science, School of Earth and Environment, University of Leeds, Leeds, LS2 9JT, UK.
Email: l.c.denby@leeds.ac.uk

**Abstract**

Two techniques are presented for characterisation of cloud-feeding coherent boundary-layer structures through analysis of large-eddy simulations of shallow cumulus clouds, contrasting conditions with and without ambient shear. The first technique is a generalisation of the two-point correlation function, where the correlation length-scale as well as the orientation can be extracted. The second technique identifies individual coherent structures and decomposes their vertical transport by the shape, size, and orientation of these objects. The bulk-correlation technique is shown to capture the elongation and orientation of coherence by ambient wind, but is unable to characterise individual coherent structures. Using the object-based approach, it is found that the individual structures dominating the vertical flux are plume-like in character (extending from the surface into cloud) rather than thermal-like, show small width/thickness asymmetry, and rise near-vertically in the absence of ambient wind. The planar stretching and tilting of boundary-layer structures caused by the introduction of ambient shear is also quantified, demonstrating the general applicability of the techniques for future study of other boundary-layer patterns.

**KEYWORDS**

coherent structures, convective triggering, methodology, moist convection, structure characterisation

## 1 | INTRODUCTION

Coherent boundary-layer structures carry perturbations of temperature, moisture, and vertical velocity necessary to trigger convective clouds, by overcoming the boundary-layer top inversion in a conditionally unstable atmosphere. However, the degree to which the spatial distribution, morphology, and perturbations carried by the coherent structures affect how clouds form is currently uncertain, as are the external drivers affecting these properties of the coherent structures. To study the formation of clouds from coherent boundary-layer structures comprehensively, we must first be able to identify and measure the properties of these structures, which is the aim of this article.

Coherent structures in the boundary layer carry so-called nonlocal (cannot simply be calculated from local scalar values) countergradient transport in the boundary

layer (Deardorff, 1966), providing transport against the vertical mean gradient of moisture and heat (in contrast to smaller turbulent eddies performing downgradient, diffusive, transport). Owing to the limited resolution available in global circulation models and numerical weather prediction models, it is necessary to parametrise the unresolved subgrid processes that provide vertical transport and lead to convective cloud formation. The development of parametrisations of nonlocal transport has been key to improving boundary-layer parametrisations (Holtslag and Moeng, 1991; Brown and Grant, 1997). Over the past two decades, the eddy-diffusivity mass-flux (EDMF) approach to boundary-layer parametrisation (e.g., Siebesma *et al.*, 2007; Rio and Hourdin, 2008; Neggers, 2009a; 2009b; Rio *et al.*, 2010) has become popular: in this approach, local turbulent transport and transport by coherent structures (leading to the formation of convective clouds) are modelled separately. However, our current lack of knowledge of how these coherent structures are affected by external forcings (ambient wind, surface heterogeneity, cold pools, etc.) and how changes in these structures affect cloud formation limits our ability to refine models of the nonlocal transport, and thus represent the genesis (formation) of convective clouds in weather and climate simulations.

As well as influencing the formation of individual clouds, these structures capture the convective state of the atmosphere, through their spatial organisation and by persisting subgrid length-scales of motion over time (a form of convective "memory"). Representation of these subgrid forms of organisation is largely absent in contemporary convection parametrisations; however, the importance of convective organisation in affecting, for example, the radiative properties of the atmosphere, and the impact of limited representation of these processes in models, is becoming increasingly clear (Bony *et al.*, 2017).

Prior work on characterising the morphology of coherent boundary-layer structures has focused primarily on measuring coherence in the boundary layer as a whole, not looking at the properties of individual coherent structures, but instead producing bulk length-scale estimates using spectral peaks in the autocorrelation and covariance spectrum to measure spatial and angular coherence (in the horizontal plane). Jonker *et al.* (1999) found in cloud-free large-eddy simulations (LES) that the shortest correlation length-scale exists in vertical velocity of the order of the boundary-layer depth, whereas the buoyancy-providing field (potential temperature $\theta$ for dry LES, virtual potential temperature $\theta_v$ when water vapour is included) typically attains larger steady-state length-scales (Jonker *et al.*, 1999; de Roode *et al.*, 2004; Salesky *et al.*, 2017). de Roode *et al.* (2004) in addition found that, for passive tracers in dry and stratocumulus-topped boundary layers, the vertical profile

of horizontal length-scales is determined by the surface to boundary-layer top buoyancy flux ratio,

$$r = \frac{\overline{w'\theta'_{vT}}}{\overline{w'\theta'_{v0}}},$$

with minimum length-scales attained when this ratio was $r \approx -0.2$ for dry convection (which is the classical buoyancy flux-ratio scale found for dry convective boundary layers) and $r \approx -1$ in the case of stratocumulus.

In simulations where clouds are present, the picture becomes more complicated for the dynamic scalars (Schumann and Moeng, 1991; de Roode *et al.*, 2004), apart from vertical velocity, which stays largely unchanged (restricted dynamically by the boundary-layer depth). The buoyancy ($\theta_v$) no longer necessarily reaches a steady-state length-scale profile, and water vapour and potential temperature produce mesoscale variability (which appears to cancel in their contributions to $\theta_v$). The length-scale characteristics found in LES have been supported through similar analysis of observations (Nicholls and Lemone, 1980; Lenschow and Sun, 2007), with the relative scales of $q$ and $\theta$ changing with the Bowen ratio, producing narrower scales for the scalar dominating buoyancy. Identifying and characterising coherent structures in observations, Schumann and Moeng (1991) found that the coherence length-scale typically peaks mid-boundary layer, where the number of structures reaches a minimum. Miao *et al.* (2006) found the plume spacing and width to be $0.7h_{BL}$ and $0.2h_{BL}$ respectively mid-boundary layer.

In place of studying correlation in inverse distance (or wavelength) space, the present work studies correlation in real space using cumulants (see history and review by Lauritzen, 2002). Cumulants have been applied by Lohou *et al.* (2000) to study thermals in a daytime boundary layer with weak wind shear over land, and characterise the influence of anisotropy on vertical transport. Schmidt and Schumann (1989) used cumulants to study coherence in the vertical rather than the horizontal plane, and identified both large-scale plumes and transient thermals in a convective boundary layer. They have also been used to expand the prognostic equations (Ait-Chaalal *et al.*, 2016) to predict correlations between fields rather than the fields themselves. In modelling by Lohou *et al.* (2000) and Schmidt and Schumann (1989), correlation is studied in real space, rather than inverse distance or wavelength space. In this work we develop this technique further by utilising cumulants and producing vertical profiles of the integral length-scale and orientation of coherence in real space.

With respect to identifying individual coherent structures in the boundary layer, prior work focused on using limit values on vertical velocity or water-vapour concentration (either separately or in combination) to

define object masks (Nicholls and Lemone, 1980; Schumann and Moeng, 1991; Grant and Brown, 1999; Berg and Stull, 2004). More recently Efstathiou *et al.* (2020) developed a masking technique to maximise the vertical transport carried by the selected region of the boundary layer. Couvreux *et al.* (2010) noted that object masks based on the physical fields (vertical velocity, water vapour, temperature) had the drawback that they capture poorly the transport through the boundary-layer top inversion and into the cloud layer, and proposed a technique based on a surface-released decaying passive tracer to track the rising boundary-layer structures. This tracer technique has been used to identify coherent structures in cloudy boundary layers (Dawe and Austin, 2012; Park *et al.*, 2016; Brient *et al.*, 2019). The current work uses the tracer, in combination with the object-splitting technique described in Park *et al.* (2018), to identify individual structures that are characterised by a prominent local maximum of vertical velocity in the boundary layer.

The aim of this article is to demonstrate the use of new techniques to characterise the morphology of coherent structures in the boundary layer and thereby provide the means to identify the properties of structures that dominate the vertical transport. We first demonstrate that using measures of spatial coherence on individual fields gives an incomplete picture of the properties of coherent boundary-layer structures, next move to characterise individual coherent structures, and later decompose the vertical transport by the structure characteristics. Using this object-based decomposition of the vertical flux, we show that the coherent structures that carry the bulk of vertical flux are plume-like rather than thermal-like (by extending from the surface and into the cloud base) and even in the absence of ambient wind have an asymmetry in their width/thickness ratio. Having the ability to measure the shape, size, and orientation of the coherent structures dominating the vertical transport will enable the study in future work of how and to what extent these properties affect how clouds form and organise, and how external factors affect the coherent structures. This in turn will enable the construction of clearer process-understanding for the coupling of clouds to the boundary layer, which ultimately can be used to build better representations of clouds in weather and climate models.

As a means of investigating the extent to which the methods discussed herein are able to unpick and quantify boundary-layer transport and its influence on clouds in different environmental conditions, we will use two simulations of shallow convection, with and without shear, as a demonstration of large-scale influence on coherent boundary-layer structures and convective clouds. The modelling setup for the simulations is discussed in Section 2. The methods used to identify coherent

boundary-layer structures and quantify their properties will be discussed in Section 3. Finally, the application of these methods will be shown in Section 4 and a discussion of this analysis will be given in Section 5.

## 2 | MODELLING SETUP

Simulations were carried out with the nonhydrostatic University of California, Los Angeles-LES model (Stevens *et al.*, 2005) with two-moment warm-rain microphysics scheme (Stevens and Seifert, 2008) on a $40 \times 40 \times 4$ km$^3$ double-periodic domain with an isotropic grid spacing of $(\Delta x, \Delta y, \Delta z) = (25, 25, 25)$ m.

The simulation setup is based on the Rain in Cumulus over the Ocean (RICO) field study (Rauber *et al.*, 2007) and associated LES model intercomparison study (VanZanten *et al.*, 2011). The RICO setup is characterised by shallow cumuli developing from moisture-dominated fluxes from the ocean surface, with the clouds constrained in growth by a prescribed large-scale subsidence aloft and large-scale advection of moisture out of the domain. In the original intercomparison study, the simulation settles into a quasisteady state after a short ($\approx 2$ hr) rapid response to the initial conditions, after which convection slowly (over $\approx 20$ hr) aggregates into larger cloud clusters by precipitation-induced cold pools. As the process leading to formation of these cloud clusters is not the focus of this study, we will be considering only the stage of cloud development before these large clusters have developed (here using $t = 6$ hr).

In this work there are two key differences from the original RICO setup as published in Seifert *et al.* (2015). Firstly, in order to study the effect of ambient wind shear on coherent boundary-layer structures, two simulations were run, one with and one without shear (see profiles in Figure 1). In the former, the wind profile from RICO was left unchanged, and in the latter the meridional and zonal wind components were set to zero. Secondly, because the near-surface horizontal velocity differs between the two simulations, the bulk aerodynamic parametrisation of surface flux was replaced with a fixed sensible ($F_s = 7$ W·m$^{-2}$) and latent heat flux ($F_v = 150$ W·m$^{-2}$), so that the two conditions have the same fluxes provided from the surface. The surface flux values were estimated from the original RICO simulation once near-equilibrium conditions have been reached (at $t \approx 6$ hr).

As seen in the horizontal cross-sections of vertical velocity in Figure 2, the presence of ambient shear causes both boundary-layer structures and clouds to become organised into elongated structures instead of convective cells. This is noticeable through the elongated line-like regions of high vertical velocity in simulations with shear,
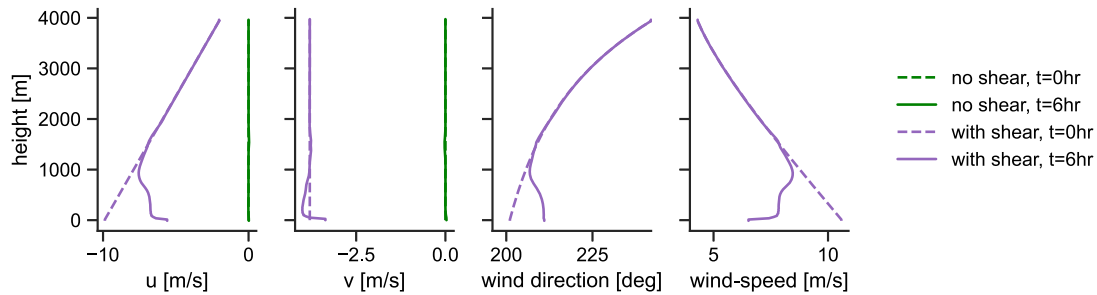
**FIGURE 1** Vertical profiles of horizontal mean wind at times $t = 0$ hr and $t = 6$ hr in meridional ($v$) and zonal ($u$) directions, together with wind direction $\phi$ (measured from $x$-axis), for cases with and without shear. The mean wind direction in the subcloud layer after $t = 6$ hr is at $\phi \approx 210°$ in the simulation with shear [Colour figure can be viewed at wileyonlinelibrary.com]
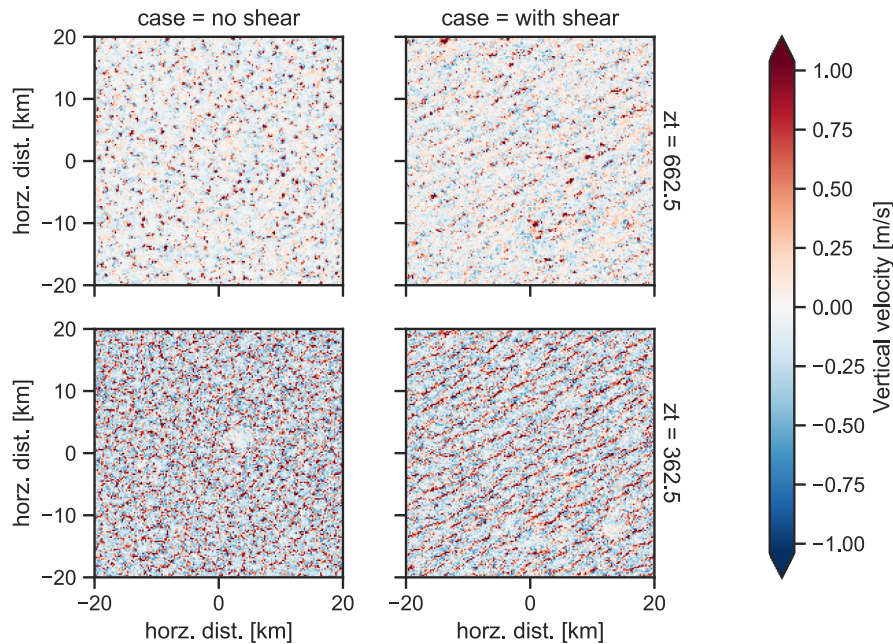


**FIGURE 2** Horizontal cross-sections of vertical velocity through the boundary-layer middle ($z \approx 362.5$ m, bottom) and at cloud-base height ($z \approx 662.5$ m, top) for simulations with shear (right) and without (left). The presence of ambient shear is clearly seen to break the geometry of convective cells and create elongated coherent boundary structures [Colour figure can be viewed at wileyonlinelibrary.com]

causing the clouds (cloud-base is at $z \approx 650$ m) to organise into structures resembling *cloud streets* instead of (as in the case without shear) at the nodes of boundary-layer convective cells. The development of cloud streets under conditions with ambient shear is consistent with prior studies (see reviews by Etling and Brown, 1993; Young *et al.*, 2002), as is the presence of sheet-like coherent structures attached to the surface extending into the bulk of the boundary layer (as in Khanna and Brasseur, 1998).

## 3 | METHODS

Before the properties of coherent boundary-layer structures that trigger clouds can be measured, it is necessary to define exactly what we mean by a coherent structure. In contrast to the cloud layer, where we can define a coherent structure purely on the concentration of water droplets, in the boundary layer there are at least three scalar fields that

carry the perturbation that eventually triggers a cloud: moisture, temperature, and vertical velocity.

We first investigate the length-scales of variability in these fields as a bulk property of the fluid. If these fields were to vary over similar length-scales, it would be relatively straightforward to define threshold criteria on either of the scalar fields that would apply to all fields. Unfortunately this is not the case (Section 3.1) and so we instead develop a method that identifies air with properties similar to that which triggers convective clouds (Section 3.2.1), by tracking air entering newly formed convective clouds.

### 3.1 | Characteristic length-scales: cumulant analysis

As an alternative to moments, cumulants provide a means to summarise the statistical correlation between one or
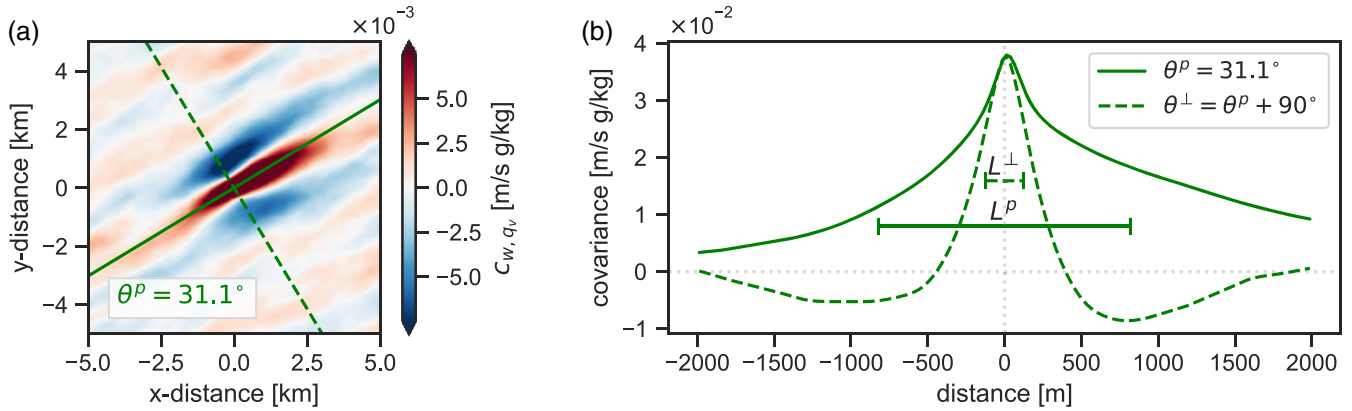
**FIGURE 3**    (a) Cumulant of vertical velocity and water vapour (i.e., the vertical moisture flux) in the horizontal plane at $z = 300$ m with principal direction of coherence identified by the red dashed line, and (b) the same cumulant sampled along (solid line) and perpendicular (dashed line) to the principal axis with characteristic (integral) widths indicated with dashed vertical lines. The elongated nature of the coherence as seen on the left is quantified by a significantly larger ($\approx 1{,}500$ versus $\approx 500$ m) characteristic length along the direction of shear. In both (a) and (b), the scaling of correlation magnitude is written above. [Colour figure can be viewed at wileyonlinelibrary.com]

more variables (Lauritzen, 2002). Similarly to Tobias and Marston (2017), where cumulants were used to identify and measure coherent structures in 3D rotating Couette flow, we here utilise the second cumulant (two-point correlation function), which for fields $\psi$ and $\varphi$ at height $z$(here $z_1 = z_2 = z$ in contrast to Tobias and Marston, 2017) is given by

$$c_{\psi\varphi}(\xi, \nu, z) = \frac{1}{L_x L_y} \int_0^{L_x} \int_0^{L_y} \psi'(x, y, z)$$
$$\times \varphi'(x + \xi, y + \nu, z) \, dx \, dy,$$

where $\psi'$ and $\varphi'$ are deviations from the horizontal mean of $\psi$ and $\varphi$ respectively, and $L_x$ and $L_y$ are the lengths of the domain in the $x$- and $y$-directions. The positions are wrapped around in the $x$- and $y$-directions, exploiting the periodic boundary conditions of the simulation.

An example of this method applied to the spatial correlation of vertical velocity ($\psi = w$) and water vapour ($\varphi = q_v$) in the middle of the boundary layer in a simulation with ambient shear is shown in Figure 3. In cases such as this, where an external forcing is causing boundary-layer and cloud structures to develop in a preferential direction, the cumulant will show increased correlation in this direction. To quantify this asymmetry we identify a *principal* and *perpendicular* direction of coherence (measured in terms of the angles $\theta^p$ and $\theta^\perp$) of the central part of the cumulant. This central part $\hat{c}_{\psi\varphi}$ is defined as the connected region at the origin with the same sign as at the origin of the cumulant $c_{\psi\varphi}$. Treating $\hat{c}_{\psi\varphi}$ as a 2D mass distribution, we then estimate the orientation angle as the principal axis (eigenvector with largest eigenvalue) of the moment of inertia tensor:

$$\bar{\bar{I}} = \begin{bmatrix} \int \hat{c}_{\psi\varphi}(\xi, \nu)\nu^2 \, d\xi \, d\nu & \int \hat{c}_{\psi\varphi}(\xi, \nu)\xi\nu \, d\xi \, d\nu \\ \int \hat{c}_{\psi\varphi}(\xi, \nu)\xi\nu \, d\xi \, d\nu & \int \hat{c}_{\psi\varphi}(\xi, \nu)\xi^2 \, d\xi \, d\nu \end{bmatrix}.$$

The cumulant can then be sampled in this horizontal plane along the principal and perpendicular directions of coherence (as seen in Figure 3, right), so that the coherence can be quantified in these directions. The presence of ambient shear is, for example, seen to cause elongation in the direction of the ambient wind (this will be discussed in detail in Section 4.1).

Once the direction of principal coherence ($\theta^p$) has been identified, a characteristic length-scale ($L^p$) of coherence may be estimated in this direction and similarly in the perpendicular direction ($L^\perp$). These length-scales are computed through a cumulant-weighted integral of distance ($l = \sqrt{\xi^2 + \nu^2}$) from the cumulant origin:

$$L_{\psi,\varphi}^\delta = \frac{\int_{-L/2}^{L/2} l \, \hat{c}_{\psi,\varphi}^\delta(l) \, dl}{\int_{-L/2}^{L/2} \hat{c}_{\psi,\varphi}^\delta(l) \, dl}, \qquad (2)$$

where $\delta \in [p, \perp]$ (for either the principal or perpendicular length-scale) and $L = \min(L_x, L_y)$ (the minimum of the simulation domain length in the $x$- and $y$-directions), with the cumulant along a particular direction, given by

$$\hat{c}_{\psi,\varphi}^\delta(l) = \hat{c}_{\psi,\varphi}(\xi = l \cos(\theta_\delta), \nu = l \sin(\theta_\delta)), \qquad (3)$$

evaluated at an arbitrary point using piecewise linear interpolation. To measure the degree of elongation, we define the *asymmetry ratio* $r_a = L^p / L^\perp$.

As well as providing a means to quantify the length-scale of correlation (and thus a single characteristic length-scale for all coherent boundary-layer structures), the shape of the cumulant can provide insight into the dynamical structure of coherent structures by quantifying the relative spatial distribution of different scalar fields. This is possible by studying two different aspects of the cumulant produced from two different fields, specifically the offset of the cumulant peak value from the origin and the skewness of the distribution around the origin. An offset of the cumulant from the origin indicates that the extreme values of two different scalar fields are located spatially offset from each other and would suggest something is driving a separation between two fields. Similarly, skewness in the cumulant distribution indicates that the two different scalar fields have differently spatially skewed distributions, e.g one field may appear spatially Gaussian, but another may be skewed relative to this. The corollary to this is that a second cumulant between two different scalar fields, which is centred on and symmetric around the origin, indicates that these two fields are, on average, spatially distributed identically (in terms of skewness) around their respective peak values and their peak values are, on average, co-located.

## 3.2 | Object-based analysis

To gain a more comprehensive understanding of transport by coherent structures in the boundary layer, we transition from looking at the boundary-layer air in a bulk sense to studying transport by individual coherent structures that may trigger clouds. This requires identifying the regions of the boundary layer that contribute to transport into convective clouds, splitting these regions into individual coherent structures, and finally formulating methods to quantify the properties of these structures.

### 3.2.1 | Object identification

To quantify the characteristic properties of individual coherent structures carrying out vertical transport, these structures must first be identified. This was achieved by first producing a 3D mask to pick out the part of the atmosphere thought to contain coherent structures, and thereafter splitting this mask into individual 3D objects.

The 3D mask was produced from the concentration of a passive tracer ($\phi$) decaying with a time-scale $\tau$, which was released from the surface (as first used in Couvreux *et al.*, 2010). Specifically, the time evolution of the tracer

is given by

$$\frac{\partial \phi}{\partial t} = -\frac{\phi}{\tau}.$$

The decay time-scale was set to $\tau = 15$ min in this study, as this represents the typical overturning time-scale of boundary-layer eddies in the simulations used (see Appendix A).

From the scalar $\phi$, a mask is created using its standard deviation in a horizontal cross-section ($\sigma_\phi(z)$) and its local deviation from the horizontal mean ($\phi'(x,y,z) = \phi(x,y,z) - \overline{\phi(z)}$), by requiring that the local deviation is $n$ standard deviations from the mean, that is, the mask $m(x,y,z)$ is given by

$$m(x,y,z) = \begin{cases} 1 & \text{if } \phi'(x,y,z) > n\ \sigma_\phi(x,y,z), \\ 0 & \text{otherwise.} \end{cases} \quad (4)$$

Here $n = 2$ was used, as this was found to produce closest agreement between the properties of air entering clouds and those identified to belong to coherent structures (see Section 4.2). The choice of decay time-scale and limit value for $n$ is similar to those ($\tau = 15$ min and $n = 2.5$) identified by Chinita *et al.* (2018) to be optimal when studying shallow moist convection in the Barbados Oceanographic and Meteorological Experiment (BOMEX) case (Siebesma *et al.*, 2003).

The constructed 3D mask was observed to identify boundary-layer air with thermodynamic properties similar to air entering into recently formed clouds (see Section 4.3 for details), making it a suitable method to separate vertical transport by local diffusive mixing (small eddies) from transport by larger, nonlocal eddies carrying fluxes leading to cloud formation.

The method of Park *et al.* (2018) was used to identify individual objects from the 3D mask. This method works by first labelling contiguous regions of the mask as *proto-objects*. These proto-objects are then further subdivided based on a second scalar field (here vertical velocity $w$) by assigning points to local maxima in the second scalar and splitting where a boundary (the "col") between two maxima has a relative value below a predefined threshold ($f = 0.7$ was used for this "col" factor, as in Park *et al.*, 2018).

To measure the thermodynamic properties of air causing the formation of clouds, individual clouds were identified from a 2D column-integrated liquid water path ($m_\mathrm{lwp}$) with a threshold value of $m_\mathrm{lwp} > 0.01$ kg · m$^{-2}$ and tracked by the spatial overlap in consecutive time-steps using the method detailed in Heus and Seifert (2013). This method identifies *active* clouds as ones with at least one buoyant core (identified from the virtual potential

temperature $\theta_v$) and *passive* clouds as those without a buoyant core. In addition, this cloud-tracking method splits clouds with multiple buoyant cores into smaller sub-clouds with the nonbuoyant regions defined as *outflow*. In this work we only consider the properties of air entering single-core *active* clouds (reaching the level of free convection, see Stull, 1985), as these are likely to have the strongest and clearest connection to boundary-layer variations. To facilitate selecting clouds that recently formed, we also keep track of the age of each cloud ($t_{age}$) by storing the time of appearance for each tracked cloud.

## 3.2.2 | Object characterisation

Once individual 3D coherent structures have been identified, a method is needed to calculate the characteristic properties of these objects. Here we detail techniques to compute the characteristic length-scales and orientation of each coherent structure.

*Topological measures: Minkowski functionals*
Instead of attempting to fit a parametrised shape (e.g., an ellipsoid) to each object with the intention of estimating an object's scale (length, width, and thickness), we instead calculate a set of characteristic scales using the so-called *Minkowski functionals* (Minkowski, 1903), which measure the topology of arbitrary structures in $N$-dimensional space (see review by Mecke, 2000 for details). These have been used in other physical applications to characterise, for example, dissipative structures in magneto-hydrodynamic turbulence (Zhdankin *et al.*, 2014), galaxy distribution (Schmalzing and Buchert, 1997), and cosmological structure formation (Sahni *et al.*, 1998; Schmalzing *et al.*, 1999). In three dimensions, the Minkowski functionals are

$$V_0 = V = \int dV, \qquad (5)$$

$$V_2 = \frac{H}{3\pi} = -\frac{1}{6\pi}\int \nabla \cdot \hat{\mathbf{n}} \, dS = \frac{1}{6\pi}\int (\kappa_1 + \kappa_2) \, dS, \quad (6)$$

$$V_1 = \frac{A}{6} = \frac{1}{6}\int dS, \qquad (7)$$

$$V_3 = \frac{1}{4\pi}\int (\kappa_1 \kappa_2) \, dS = \chi, \qquad (8)$$

where $\hat{\mathbf{n}}$ is the surface normal, $\kappa_1$, $\kappa_2$ are the maximum and minimum local curvature, and $\chi$ is the Euler charac-

teristic (essentially related to the number of holes through an object). To evaluate these integrals numerically on the discrete output from the large-eddy simulations, we use Crofton's formula (see Appendix B), which provides discrete approximations for terms (for example the surface normal) that are otherwise difficult to evaluate on objects constructed from individual cubic volumes of the simulation underlying grid. For reference, the Minkowski functionals for a parametrised spheroid and ellipsoid will be shown, using the analytical expressions (where available, and otherwise numerical integration) for surface area and mean curvature given in Schmalzing *et al.* (1999) and Poelaert *et al.* (2011).

From these functionals, Schmalzing *et al.* (1999) define a characteristic *length* ($L_m$), *width* ($W_m$), and *thickness* ($T_m$) given by

$$L_m = \frac{3V_2}{4V_3}, \qquad W_m = \frac{2V_1}{\pi V_2}, \qquad T_m = \frac{V_0}{2V_1}, \qquad (9)$$

named as such because, by construction, $L_m \geq W_m \geq T_m$ is guaranteed for any convex body. The coefficients scaling the Minkowski functional ratios in these expressions are derived such that all three length-scales equal the radius when applied to a sphere. Note that, for objects with one or more holes, $V_3 = \chi \leq 0$ and so the length will not be evaluated for these objects. The length, width, and thickness may be summarised further by computing the *filamentarity* ($F_m$) and *planarity* ($P_m$):

$$F_m = \frac{L_m - W_m}{L_m + W_m}, \qquad P_m = \frac{W_m - T_m}{W_m + T_m}, \qquad (10)$$

which in turn indicate whether an object is more *stick*-like (large filamentarity) or *pancake*-like (large planarity), with filamentarity being large when the object is much larger than it is wide (and thick) and planarity being large when an object is very thin compared with both its width and length.

The Minkowski functionals thus enable the quantification of an object's shape, making it possible to, for example, investigate whether objects that are the primary contributors to vertical transport have a characteristic shape, which can be used to inform the formulation of an integral model for representing this transport.

To provide a reference for the range of values that may be expected for coherent structures in the atmospheric boundary layer, Figure 4 is a filamentarity versus planarity plot for a number of synthetically created, numerically integrated, sheared, and stretched spheroids. The length (through the centre of the structure) was kept constant across all shapes while varying the width and shearing
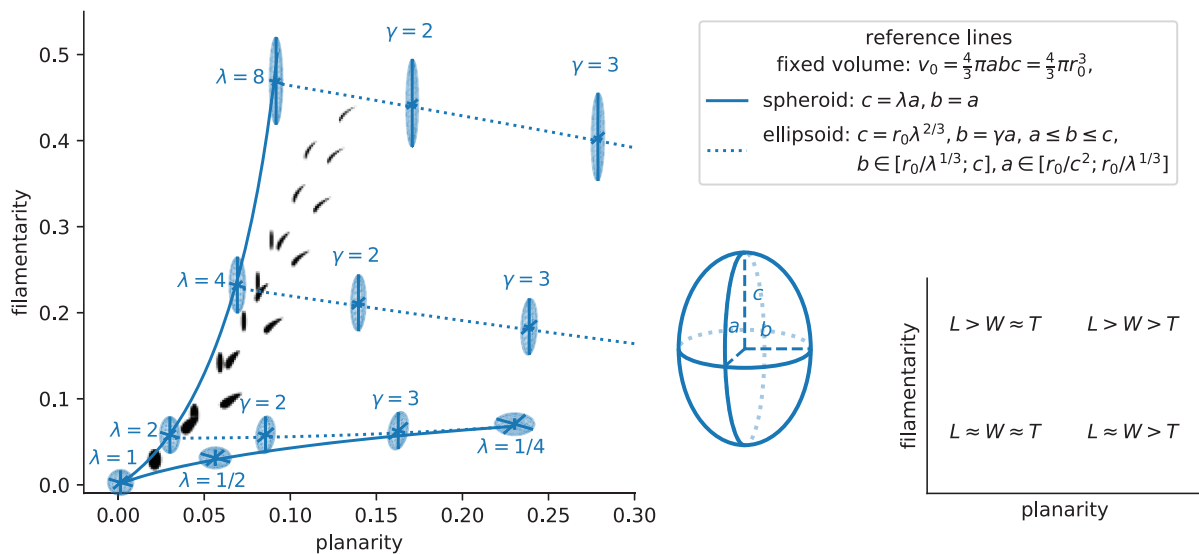
**FIGURE 4** Filamentarity versus planarity plot for synthetically created 3D thermal structures with centreline length 500 m and varying shear and distance (left). For each structure, the data point is marked with a vertical cross-section (black). Two sets of reference lines are given using analytical solutions to the Minkowski functionals of a spheroid (solid blue) and ellipsoid (dotted blue). $\lambda$ parametrises the aspect ratio of the spheroid semi- and major axis. $\gamma$ parametrises the deformation of a spheroid with a fixed value $\lambda$ and fixed major axis, by varying the remaining two axes (with aspect ratio $\gamma$). The filamentarity–planarity values effectively enable the projection of an object's length ($L$), thickness ($T$), and width ($W$) into two coordinates (right) [Colour figure can be viewed at wileyonlinelibrary.com]

distance. Each data point is marked by an outline of the shape's structure by plotting the vertical cross-section through each shape's symmetry plane. As a means of reference for the numerically integrated shapes, the analytical functions for filamentarity and planarity are plotted for a spheroid, by integrating the analytical forms of the Minkowski functionals for a spheroid while varying the aspect ratio between one axis and the two others. In addition to the spheroid reference lines, the deformation of a spheroid through a general ellipsoid while keeping the volume and major axis length constant is provided, including the aspect ratio of the two remaining axes as $\alpha$. It can, for example, be seen that a prolate spheroid with $\lambda = 2$ becomes an oblate spheroid with $\lambda = 1/4$ (the Minkowski functionals are independent of orientation, which will be dicussed next).

*Object tilt and orientation*

As the Minkowski functionals (detailed in the previous section) only provide measures of scale, but not orientation, of individual objects, we introduce a means of calculating the $xy$-plane orientation ($\phi$, measured from the $x$-axis) and tilt ($\theta$, measured from the $z$-axis) of an individual object (see Figure 5). The characteristic tilt and orientation for an individual coherent structure is calculated by first forming a *centreline* through the centroids of vertically adjacent slices of a given structure, and then computing the area-weighted angular average of $z$-tilt and
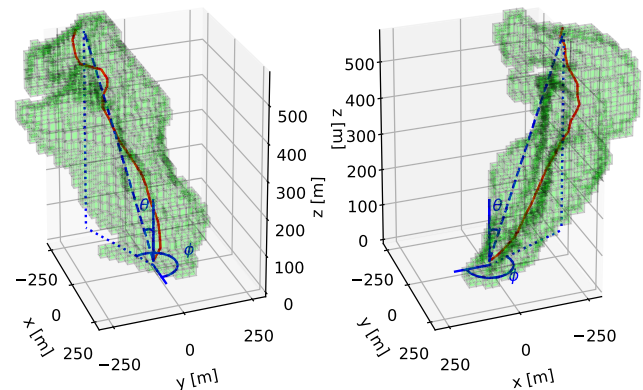


**FIGURE 5** Voxel-rendering of single coherent structure from sheared simulation from two viewing angles, with object orientation angles $\theta$ (tilt from $z$-axis) and $\phi$ ($xy$-orientation from $x$-axis) and centreline (red) indicated [Colour figure can be viewed at wileyonlinelibrary.com]

$xy$-orientation along this centreline (see Appendix C for details).

## 4 | RESULTS

In this section we analyse the sheared and nonsheared simulations using the methods detailed above. The analysis first focuses on extracting characteristic length-scales of different fields in the boundary layer as a whole, without attempting to identify individual coherent
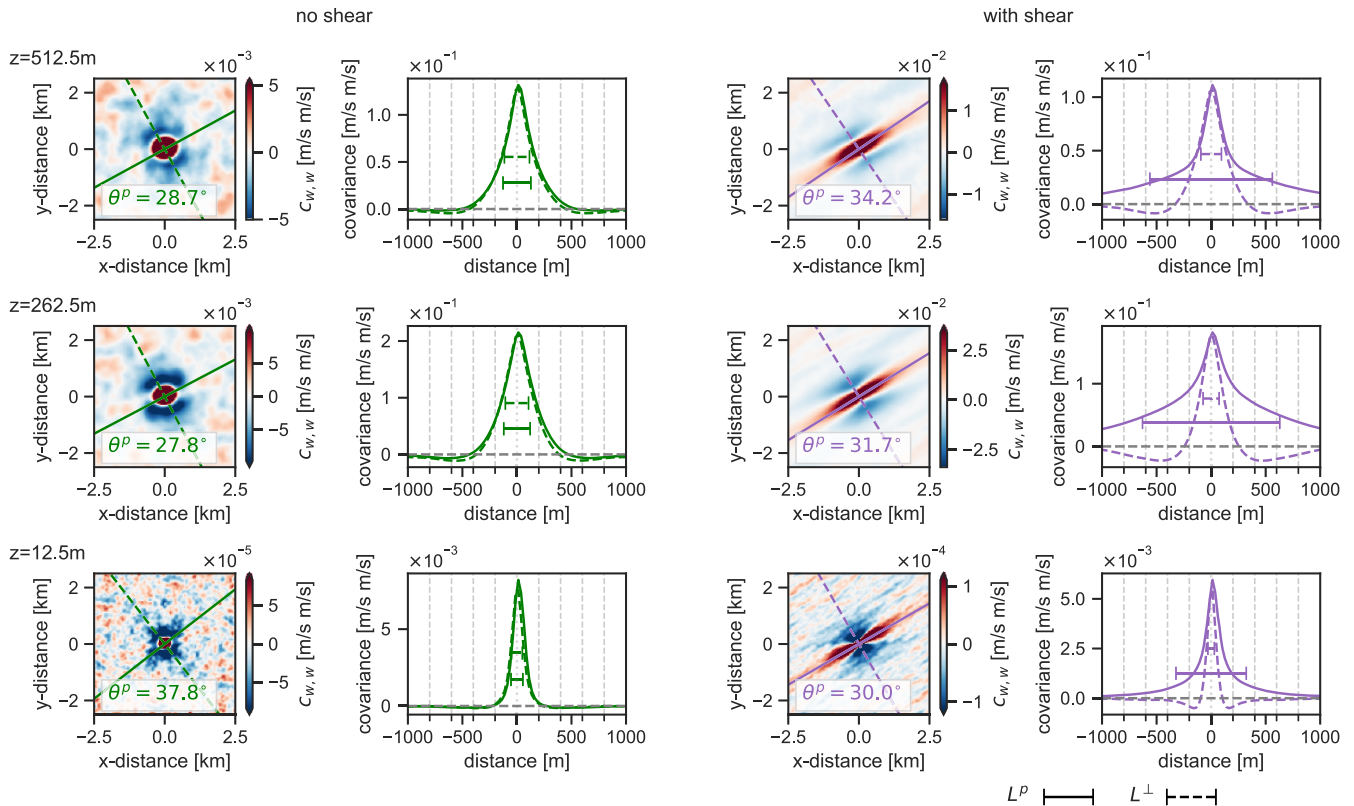
**FIGURE 6** Second cumulant of vertical velocity with vertical velocity at increasing heights in the boundary layer in simulations without shear (leftmost two columns) and with shear (rightmost two columns). At each height, the cumulant (left, measuring coherence as a function of distance) is associated with the same cumulant sampled along the identified principle and perpendicular direction of coherence (right), with the calculated coherence length-scale indicated by solid and dashed range markers. Note the magnitude of coherence changes with height. For each subfigure, the scaling of the correlation magnitude is written above [Colour figure can be viewed at wileyonlinelibrary.com]

structures. Later, the boundary-layer air that is likely to be feeding convective clouds is identified. Lastly, properties of *individual* coherent structures are studied with the aim of revealing the properties of coherent structures that dominate the vertical moisture flux. We focus here on the moisture flux, as the simulations represent convection over the ocean and so have a low Bowen ratio. Similar analysis may be carried out for heat flux in conditions of high Bowen ratio.

## 4.1 | Vertical profiles of characteristic horizontal scales

To study the vertical transport produced by coherent structures in the boundary layer, we must first formulate how to define these structures. Unfortunately the different scalar fields connected with transport relevant to moist convection (vertical velocity, buoyancy, moisture, and heat content) vary on very different length-scales and these scales change with height in the boundary layer. To demonstrate this variability, Figures 6 and 7 show the second cumulant

of vertical velocity with itself ($c_{w,w}$, the autocorrelation) and the second cumulant of vertical velocity and liquid water potential temperature ($c_{w,\theta_l}$) in the horizontal plane mid-boundary layer ($z = 300$ m).

Considering first the autocorrelation of vertical velocity ($c_{w,w}$), we note that vertical velocity features are elongated with ambient shear and axisymmetric without shear, as expected. The coherence length-scale (slashed vertical line) is largest in the middle of the boundary layer where vertical velocity peaks, before thermals are decelerated, becoming negatively buoyant in the relatively warm and dry layer below the cloud.

Considering instead $c_{w,\theta_l}$, there is narrow length-scale of positive correlation until $z \approx 200$ m, embedded within a larger-scale negative correlation. The positive correlation is provided by buoyancy, in turn induced by sensible surface heat fluxes. However given that RICO represents shallow convection over the ocean (making the Bowen ratio small), the buoyancy becomes dominated by water vapour and, above $z \approx 200$ m, the correlation with potential temperature becomes negative. This transition causes the correlation length-scale to increase with
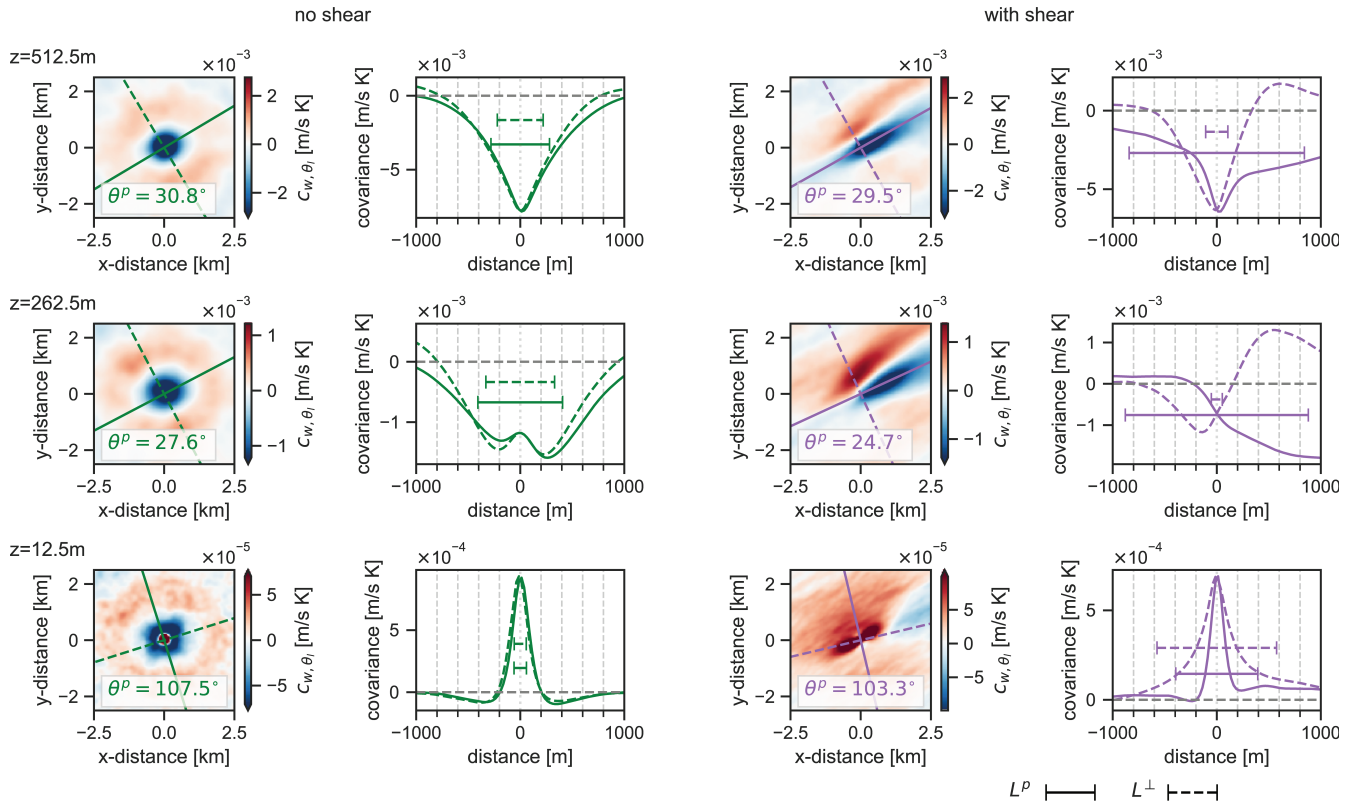
**FIGURE 7** Second cumulant of vertical velocity with liquid water potential temperature (panels as in Figure 6) [Colour figure can be viewed at wileyonlinelibrary.com]

height until $z \approx 200$ m, above which the larger-scale negative correlation takes over. In simulations with ambient shear, the correlation between vertical velocity and temperature is not only elongated in the direction of the shear, but asymmetric in the direction of the shear (evidenced by the skewness and offset of the correlation). This means that potential temperature features are displaced in the downwind direction relative to the vertical velocity, suggesting that similarity solutions that assume radially symmetric distributions of different scalar fields (i.e., all scalar fields are assumed to be a function of a single radius $r$), as most plume-based models do (e.g., Devenish et al., 2010), may not be valid in conditions where shear is present.

To examine the variation in correlation length-scale with height, the cumulant-based coherence calculation was carried out at every model level in the boundary layer. Figure 8 shows the integral cumulant length-scale as a function of height, in the direction of strongest correlation ($L^p$) and perpendicular to this ($L^\perp$), for both the sheared and nonsheared simulations. In the discussion below, subscripts "S" and "NS" will be used to denote properties extracted from the sheared and nonsheared simulations respectively. Comparing first the characteristic length-scales across different fields, the vertical velocity is

consistently confined to narrower features, whereas moisture and sensible heat organise on larger scales (consistent with de Roode et al., 2004). The characteristic length-scale of the radioactive tracer field is generally larger than that for vertical velocity, possibly owing to the tracer concentration retaining high values in overturning vortices of thermals, within which the vertical velocity becomes negative.

In the direction of strongest correlation (superscript $p$), in both simulations, with and without shear (though more prominent with shear), the vertical velocity length-scale increases with height from the surface as thermals are accelerated by the buoyancy provided through surface fluxes, reaching a maximum scale of $L^p_{w,w}|_{NS} \approx 300$ m and $L^p_{w,w}|_S \approx 1,300$ m at $z \approx 400$ m. Above this height, the velocity scale decreases with height, as the buoyancy of the rising coherent structures becomes negative and the structures begin decelerating through the convective inhibition layer. This effect of buoyancy on the correlation length-scale is more clearly seen when investigating the cross-correlations with vertical velocity (see below). Comparing the moisture and virtual liquid potential temperature (buoyancy) length-scales with the radioactive tracer, it is notable that, although the buoyancy is water-vapour dominated (the surface-flux Bowen
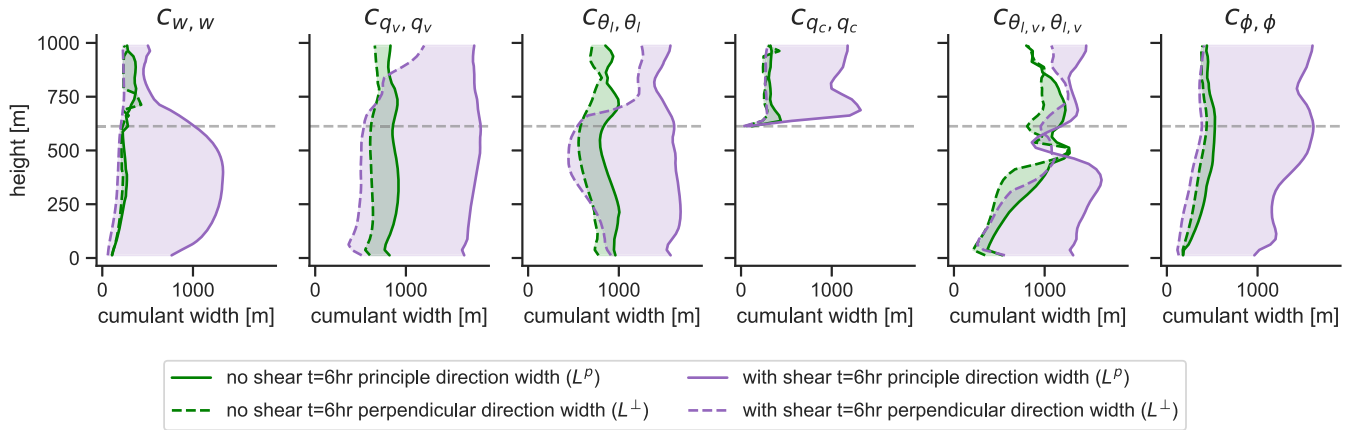
**FIGURE 8** Horizontal coherence length-scales in the direction of strongest coherence ($L^p$, solid lines) and perpendicularly to this ($L^\perp$, dashed lines) of vertical velocity ($w$), water vapour ($q_v$), liquid water potential temperature ($\theta_l$), cloud water ($q_c$), virtual liquid water potential temperature ($\theta_{l,v}$) and the radiative passive tracer ($\phi$), for simulations with shear (purple lines) and without shear (green lines) [Colour figure can be viewed at wileyonlinelibrary.com]

ratio is low), the length-scales of correlation of water vapour ($L^p_{q_v,q_v}|_{NS} \approx 800$ m and $L^p_{q_v,q_v}|_S \approx 1,800$ m at $z \approx 300$ m) are significantly larger than those of both the radioactive tracer ($L^p_{\phi,\phi}|_{NS} \approx 400$ m and $L^p_{\phi,\phi}|_S \approx 1,200$ m at $z \approx 300$ m) and the buoyancy features ($L^p_{\theta_{l,v},\theta_{l,v}}|_{NS} \approx 800$ m and $L^p_{\theta_{l,v},\theta_{l,v}}|_S \approx 1,400$ m at $z \approx 300$ m) in the lower half of the boundary layer (until $z \approx 300$ m). This means that larger-scale water-vapour variability is producing buoyancy on a shorter length-scale, which in turn is accelerating boundary-layer air on an even shorter length-scale. This is important for modelling, as the variability of the buoyancy scalar (here water vapour) cannot simply be used to infer the scale of coherent rising structures. Lastly, the maximum correlation length-scale of cloud water (a measure of cloud size) is of the order of $L^p_{q_c,q_c}|_{NS} \approx 400$ m and $L^p_{q_c,q_c}|_S \approx 1,500$ m at $z \approx 650$ m (near cloud base), showing most similarity to the radioactive tracer coherence length-scale at cloud base.

The direction of longest correlation distance (see Figure 9) is, for all fields (including cloud water), oriented with the ambient wind direction, which is also the principle direction of shear, throughout the boundary layer and into the cloud base. In the absence of shear, some fields demonstrate some degree of turning with height, but the low degree of asymmetry ($r_a < 2$ at all heights) suggests that there is very little direction to the correlation and, on examining multiple time steps, the direction of correlation was seen to be a transient feature, so that no preferential orientation can be discerned. Perpendicular to the direction of strongest correlation, the cumulant length-scale ($L^\perp$) is similar for simulations both with and without shear, suggesting that the boundary-layer thermals (and clouds) show similar vertical dynamical evolution in the direction perpendicular to the wind shear.

Applying the same analysis to the vertical fluxes of heat, moisture, buoyancy, and radioactive tracer (Figure 10), we see that these features are generally narrower than the scalar being transported, suggesting that the scale of vertical velocity is dominating the length-scales of vertical transport. All flux fields show clear elongation by ambient shear. The heights at which the correlation is negative are marked by minus-sign markers ("−"), showing again the transitions for heat (at $z \approx 200$ m the heat flux changes sign) and buoyancy (at $z \approx 500$ m rising structures are no longer buoyant) where the correlation length for both collapses. The moisture and radioactive tracer flux correlations ($c_{w,q_v}$ and $c_{w,\phi}$) have near-monotonic increases in size with height until cloud base is approached.

## 4.2 | Cross-correlation of scalar fields

As shown above, different scalar fields show different length-scales of coherence and we now turn to investigating the extent to which these fields are correlated, not in space but in the distributions of their scalar values. In Figure 11, for the simulations with (right) and without shear (left), the joint distribution of water vapour and potential temperature through horizontal cross-sections at increasing heights are plotted. At each height a bivariate histogram was created, the bins ranked by number of points, and contours drawn around the bins with 10% (inner contour, solid lines) and 90% (outer contour, stippled lines) cumulative point count. Constructed in this way, the set of contours at each height identify the centre and width of the joint distribution for the scalar fields visualised (forming a 2D *box-and-whisker* plot). For reference, the boundary-layer mean values for potential temperature
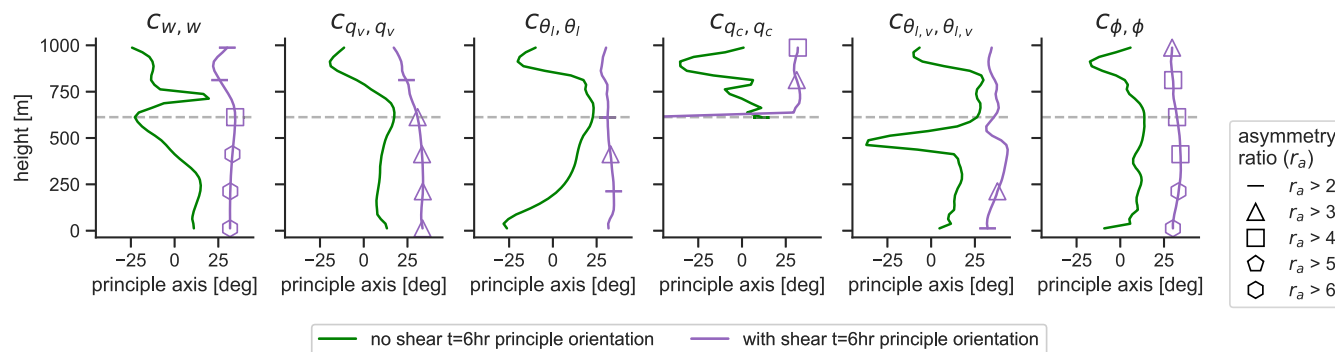
**FIGURE 9**  Direction of longest coherence as angle from *x*-axis (for the variables shown in Figure 8) with the degree of asymmetry given every 200 m by the marker symbol. In the presence of ambient shear, all fields are elongated in the direction of shear. In particular, note that cloud structures (forming at $z \approx 650$ m) are elongated in the same direction as boundary-layer structures [Colour figure can be viewed at wileyonlinelibrary.com]
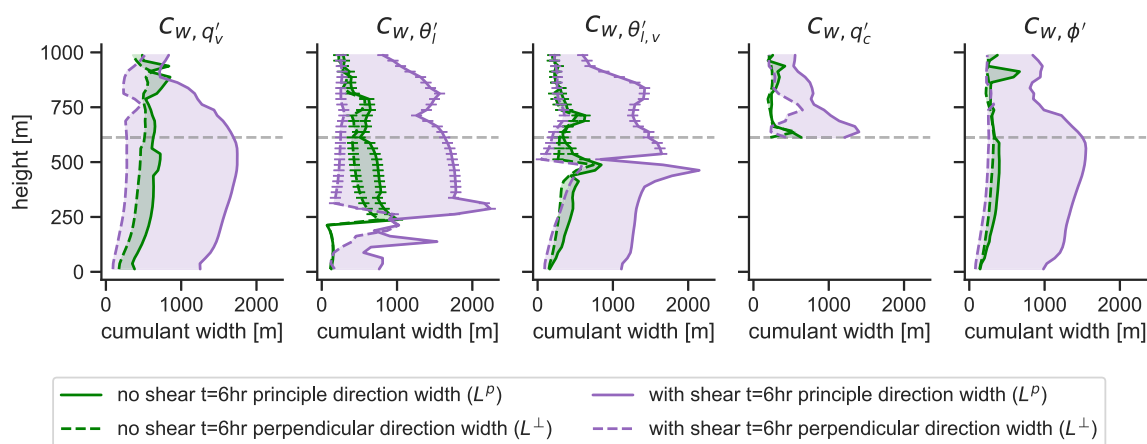


**FIGURE 10**  Horizontal coherence length-scales, in simulations with (purple lines) and without (green lines) shear, of vertical velocity with water vapour, liquid water potential temperature, buoyancy (virtual liquid water potential temperature), cloud condensate, and radioactive tracer effectively producing a coherence length-scale for the vertical flux for each scalar field. Heights at which anticorrelation occurs are marked with a minus sign ("−") [Colour figure can be viewed at wileyonlinelibrary.com]

and moisture are included. In addition to the distributions in horizontal cross-sections, the joint distribution for points immediately below (grid spacing $\Delta z = 25$ m) newly formed ($t_{age} < 3$ min) clouds (identified by cloud tracking) is included.

The distributions have similar characteristics in the two simulations; near the surface, the boundary layer is warm and moist relative to the boundary-layer mean; through the superadiabatic near-surface the distribution rapidly becomes cooler and drier with height (until $z \approx 100$ m). With further increase in height, the distribution is stretched to drier and warmer values, as mixing with warm dry air subsiding through the boundary-layer top has an increasing influence.

In both simulations, the distribution of air entering newly formed clouds (in red) coincides with the coldest and most humid part of the boundary-layer joint distribution. The cloud-base distribution contains

a larger range of moisture values in the simulation with shear, including drier parts of the bulk of the boundary-layer distribution. This may be because ambient shear increases mixing into the rising coherent structures, carrying drier air in the regions with high vertical momentum, or because the lower overall virtual potential temperature (buoyancy) of the boundary layer causes more air to be buoyant enough to rise to the level of condensation.

In addition, the distributions in the two simulations differ through a translation in potential temperature by approximately $\approx 0.1$ K, which, although small, is of the order of the width of the distributions in both cases. This suggests that in the presence of shear there is a stronger transport of heat out of the boundary layer and into the cloud layer. This offset indicates that, even in conditions where the prescribed surface fluxes are exactly the same, the dynamics of boundary-layer transport can vary to a
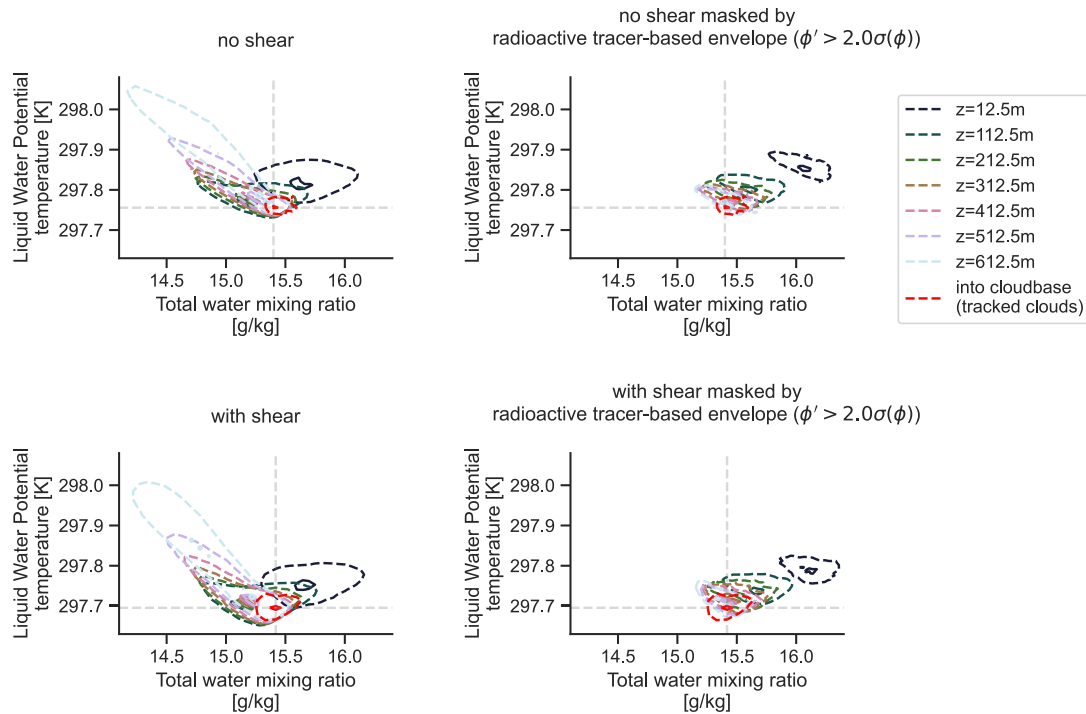
**FIGURE 11**    Joint distributions of total water vapour specific humidity and liquid potential temperature (same as potential temperature in the subsaturated boundary layer below cloud) in horizontal cross-sections at increasing heights in the boundary layer, together with properties of air entering through cloud base of newly formed ($t_{age} < 3$ min) clouds in simulations with (bottom) and without (top) shear, both without (left) and with (right) the radioactive tracer mask applied. For each height and at cloud base, the inner and outermost contours identify the regions that cumulatively contain the 10% and 90% highest point density, with the number of bins in $\theta_l$ and $q_t$ scaling by the number of points, $N_{bins} = (N_x \times N_y)^{1/4}$. Grey slashed lines are centred on the peak of distributions for cloud-base entering air. From a relatively moist and warm near-surface state, the distribution first dries and cools into the bulk of the boundary layer, then warms and dries with height as air subsiding through the boundary-layer top imparts a stronger influence [Colour figure can be viewed at wileyonlinelibrary.com]

degree that alters the property of air that forms clouds, and so thresholds based solely on the thermodynamic fields (e.g., $\theta_l$ and $q_t$) are inadequate in identifying air that will form clouds.

It is clear from these joint distributions that, if the aim is to characterise coherent structures that actually cause the formation of clouds, it is inadequate to simply construct a conditional sampling based on threshold values of the scalar fields causing transport. Instead a method that tracks air transported from the surface layer and into cloud is required and, to achieve this, in the next section we employ a radioactively decaying tracer.

## 4.3 | Identifying cloud-feeding coherent structures

We now turn to characterising the coherent structures that have the potential to trigger clouds. This is done by first verifying that the air-mass selected by conditional sampling using the decaying passive tracer (see Section 3.2.1 for details) has thermodynamic properties similar to air entering newly formed clouds. Secondly, we examine the

vertical moisture transport by individual coherent structures (identified by splitting the conditionally sampled air) as a function of the vertical extent of each structure. This flux decomposition will show that, for coherent structures identified using the decaying passive tracer, it is the structures that extend from near the surface through cloud base and into cloud that carry the bulk of the vertical moisture transport, suggesting that the clouds manifest as billowing tree-crowns sat atop trunks of continuous transport.

Examining first the thermodynamic properties of air sampled using the decaying passive tracer, the joint distributions of the previous section are conditionally sampled (Figure 11, right), by requiring that the concentration of decaying passive tracer is at least two standard deviations from the horizontal mean (see Section 3.2.1 for details). Using this method for both the sheared and nonsheared simulations, the distributions collapse down to align near-perfectly with that of air entering through cloud base, indicating that the radioactive tracer is picking exactly the air that may trigger clouds. In addition, for both cases the means of the distributions appear to be near-linearly translated with height, suggesting that
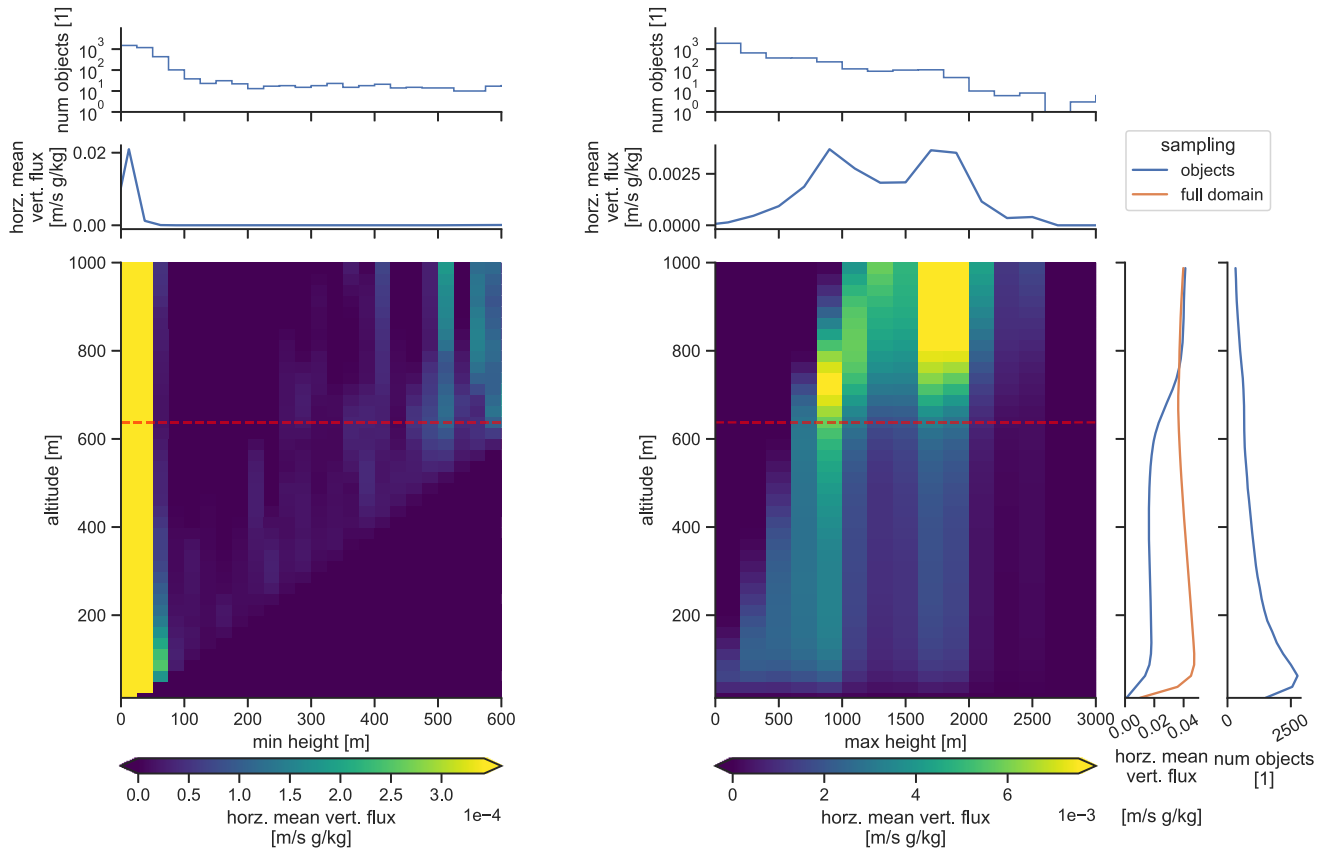
**FIGURE 12** Vertical moisture flux decomposed by height and object vertical extent, decompositing by minimum height (left) and maximum height (right) of each object in the simulation without shear, with mean flux vertical profiles given as right marginal plots, and boundary-layer mean flux and object number distribution as top marginal plots. In the moisture flux profile, the total domain mean (orange) is shown together with the moisture flux contributed by the selected objects (blue). The flux is carried, in aggregate, primarily by objects extending from the surface and into the cloud layer, providing flux throughout the boundary layer [Colour figure can be viewed at wileyonlinelibrary.com]

these coherent cloud-triggering structures mix with the bulk of the boundary layer at a similar rate for both potential temperature and water vapour. Finally, the widths of the joint distributions appear nearly unchanged with height. All of these facts are encouraging for the prospect of parametrisation of the mixing into coherent updrafts in the boundary layer, by which the properties of cloud-triggering air may be predicted based on the surface fluxes (and other external forcing factors).

Although the radioactive tracer method identifies air with the same statistical properties as air that is triggering clouds, it is not guaranteed that every volume of this boundary-layer air will actually trigger a cloud. Some structures may simply be too small to survive the journey to the condensation level without being completely mixed into the bulk boundary-layer air. This can be addressed in further work by tracking boundary-layer structures and identifying which ones actually trigger clouds (beyond the scope of this study). Here, we instead identify the structures that dominate the vertical moisture transport.

We examine this next by decomposing the moisture flux at a given height by the vertical extent (measured as the height of the bottom $z_{min}$ and the top $z_{max}$) of coherent structures contributing to the flux in Figure 12. Simulations both with and without shear show the same structure, and so we only show the situation without shear here. Note that an individual object of a given vertical extent will likely contribute to the flux at a number of different heights and the figure simply shows, at any given height, how low (Figure 12, left) or high (Figure 12, right) structures that contribute to the flux extend.

Considering first the flux decomposition by the minimum height of each coherent structure (Figure 12, left) we find that almost all flux is carried by structures extending down to the surface ($z \approx 100$ m), even though this accounts for only half the number of coherent structures. Considering secondly the maximum height of the coherent structures, we find that $\approx 90\%$ of the moisture flux through the boundary layer is transported by structures that extend above cloud base ($z_{cb} \approx 650$ m), transporting moisture all
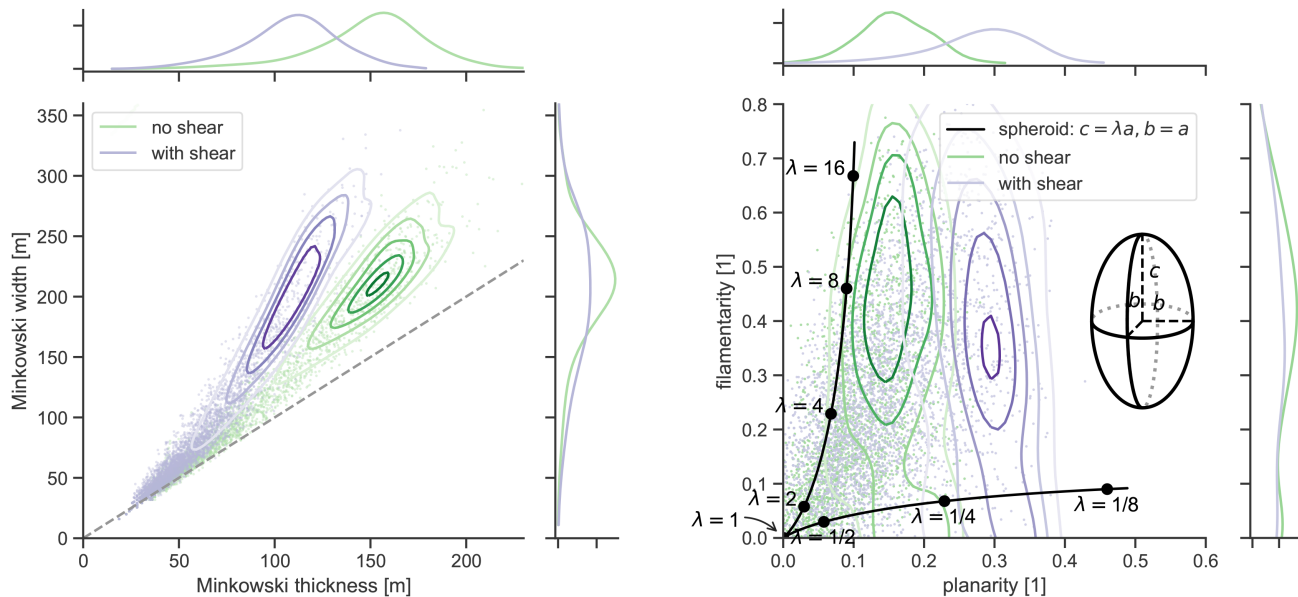
**FIGURE 13** Minkowski functional derived width versus thickness (left) and filamentarity versus planarity (right) of individual objects (points) for the cases with (green) and without (purple) shear. The contours depict the distribution of vertical moisture flux with these object characteristics (computed as a flux-weighted probability density function constructed using Gaussian kernel density estimation). In the filamentarity versus planarity plot, a spheroid is given as reference (solid black) with independent axis parametrised by $\lambda$ and deformation of a spheroid through a general ellipsoid with fixed major axis and varying aspect between the remaining two axes ($\alpha$) [Colour figure can be viewed at wileyonlinelibrary.com]

the way from near the surface into and through cloud base. The flux is dominated by structures terminating at $z \approx$ 900 m with a second peak at $z \approx 1,800$ m, possibly accounting for clouds reaching and passing the height of free convection (*forced* and *active* clouds as denoted by Stull, 1985). From the above analysis, we conclude that the most appropriate model for representing transport in the boundary layer is a plume rather than a thermal, the latter providing near-continuous transport with height extending from the surface into cloud base (see, e.g., Houze and Houze, 2014). This pictures still holds (though not shown here) if the decaying tracer threshold is increased (narrowing the structures).

The above analysis also shows that, were we to characterise coherent structures solely by the passive tracer, we would be characterising in part the properties of structures performing transport in cloud. As we are concerned here primarily with the characteristics of structures that effect transport below cloud, we will in later sections crop structures at cloud base so that only the subcloud part is considered.

## 4.4 | Minkowski characteristics of coherent structures

Having identified the below-cloud coherent structures with correct thermodynamic properties (for triggering clouds) and carrying the majority of the vertical moisture,

we next calculate characteristic properties of each structure and decompose the boundary-layer moisture flux by the object scales, to ascertain the characteristics of structures dominating the flux. This flux decomposition is visualised as a (boundary-layer mean) moisture-flux weighted probability density distribution (PDF) (computed using Gaussian kernel density estimation (KDE): Jones *et al.*, 2020), with weights given by the per-object total moisture flux and the PDF computed over the object characteristics used in the decomposition. To demonstrate the effect of external forcing, the characteristics of structures dominating the flux in the simulations with and without shear will be contrasted. To do this, we calculate a characteristic length, width, and thickness for each object using the so-called Minkowski functionals (detailed in Section 3.2.2).

We first examine the boundary-layer moisture flux when decomposed by the width and thickness of the coherent structures (Figure 13, left) with contours in purple and green depicting the distribution in cases with and without shear respectively. The scatter plot, depicting the width and thickness of each structure, shows that the majority of structures are small and nearly axially symmetric (appear near the unit line). However, once we consider the contribution to the vertical moisture flux, the larger and more asymmetric structures dominate. This result is in contrast to the cumulant analysis (Section 3.1), which indicated no global horizontal orientation of coherent structures in the absence of ambient wind. This may be

due to the geometry of cellular convection (in the absence of wind) imprinting on the flux-carrying coherent structures. This asymmetry is more pronounced when ambient shear is present, shifting the width/thickness ratio from $\approx 150\,\text{m}/200\,\text{m} = 3\text{:}4$ to $\approx 100\,\text{m}/200\,\text{m} = 1\text{:}2$.

This asymmetry can be succinctly captured by computing the filamentarity and planarity (measuring how *pencil*-like or *disc*-like object each is), as seen in Figure 13, right, showing that ambient shear causes the coherent structures to be stretched planar, which can be seen by a $\approx 100\%$ increase in planarity from $P_{\text{NS}} \approx 0.15$ and $P_{\text{S}} = 0.35$. As a reference (in black), the filamentarity and planarity of an ellipsoid with varying elongation (parametrised as the aspect ratio between one axis and the remaining two), the coherent structures can be seen to move from being more cylindrical to sheet-like in shape. Here only structures with Euler characteristic $\chi = 1$ (objects without holes) are considered (as the length is otherwise not defined). Although objects with holes do contribute a significant fraction of the moisture flux ($\approx 20\%$ and $\approx 70\%$ for the cases without and with shear respectively), this fraction is reduced when the passive tracer threshold is increased (to $\approx 4\%$ and $\approx 30\%$ for $\phi = 3$) and the relative stretching between the two cases becomes more pronounced (not shown here). It is possible that applying a lower object-splitting threshold ($f$) will reveal that these objects with holes should in fact be considered as very closely spaced rising thermals, something that can be considered in future work.

## 4.5 | Object orientation

In addition to knowing the characteristic length-scales and shape of individual coherent structures, it is instructive to determine the tilt and orientation of each object in order to be able to formulate an integral model to represent transport by coherent structures. In Figure 14, the vertical moisture flux has been decomposed by the tilt and orientation angles of all subcloud objects present at $t = 6\,\text{hr}$ in simulations both with and without shear. This shows that the presence of ambient shear ($\approx 2\,\text{m} \cdot \text{s}^{-1}$ change in wind speed over the subcloud layer) caused the mean tilt of individual objects to change from $\theta_{\text{no,shear}} \approx 15°$ (near-vertical, given the near-symmetrical angular spread in orientation angle) to $\theta_{\text{shear}} \approx 40°$ and changed the structures from having no preferential horizontal orientation to being oriented with the direction of wind shear ($\phi_{\text{shear}} \approx 210°$).

This direction of orientation in the presence of ambient wind was found to coincide with the principle direction of coherence identified using cumulants (Section 4.1). Being able to quantify the stretching and tilting of individual structures is an improvement on the measure of elongation provided by using cumulants, as we are able to separate
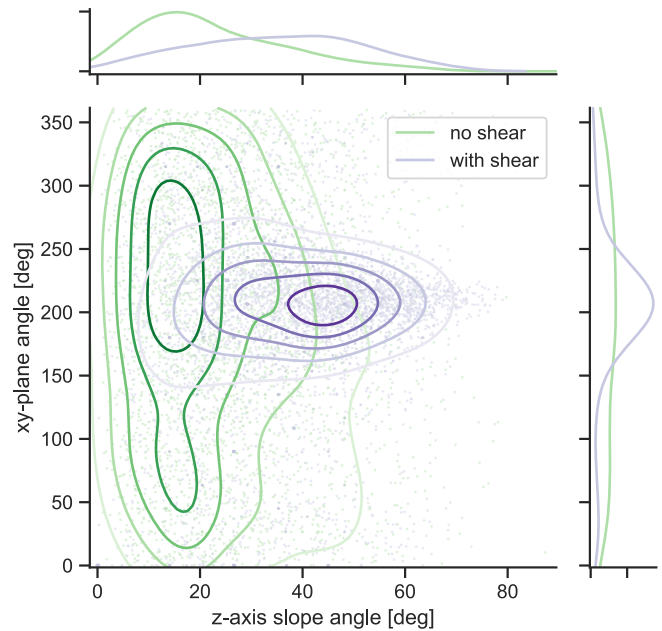


**FIGURE 14** Vertical moisture flux decomposed (as in Figure 13) by *xy*-orientation angle ($\phi$) against *z*-axis slope angle ($\theta$) of coherent structures present at $t = 6\,\text{hr}$ in simulations with (purple) and without shear (green), together with distributions in each along plot margins. Note that the drop-offs in the distribution of *xy*-plane orientation angles near $\phi = 0°$ and $\phi = 360°$ are an artefact of using Gaussian KDE estimation of the underlying distribution. This was not remedied by copying data to mimic the cyclical nature of $\phi$, as the Gaussian KDE method leads to excessive smoothing on nonunimodal data [Colour figure can be viewed at wileyonlinelibrary.com]

out cumulant elongation due to individual structures from that caused by structures being spatially organised into linear features.

## 5 | DISCUSSION

The two methods presented here, the first focusing on bulk measures of coherence in the boundary layer (using cumulants) and the second on identifying and quantifying morphological properties of flux dominating individual coherent structures (using Minkowski functionals and tilt/orientation calculation), have complementary strengths.

The principal difference between the two approaches is that the cumulant-based method produces a length-scale estimate through considering the spatial coherence throughout the fluid, whereas identifying and characterising individual objects gives an estimate of scale for individual coherent structures. Two individual objects in close proximity will increase the cumulant length-scale estimate, meaning that the cumulant length-scale conflates the object size and spatial organisation of objects

(specifically the interobject distance). In addition, in cases where there are multiple populations of coherent structures, the cumulant method will conflate these into one integrated measure and the relevant details of each separate population may be lost. In particular, in the upper part of the boundary layer, which is characterised by ascending buoyant thermals and descending entrainment flows, the cumulant analysis will not necessarily give a "clean" description of either of these.

Another aspect in which the two approaches differ is how the cumulant method estimates length-scales in the horizontal plane (the method requires translational symmetry to study coherence as a function of displacement and so cannot be applied vertically without picking a reference height), whereas the Minkowski length-scales of individual objects are not constrained in the orientation in which these length-scales are calculated. This means that the two measures of length cannot be compared directly, as the Minkowski length-scales are not measured in the horizontal plane and necessitate the calculation of object orientation to interpret the length-scales calculated. It further means that the cumulant-based measure of scale cannot separate out the orientation of individual structures from the orientation of spatial organisation in general. The degree of tilt could, however, be measured with cumulants by computing the correlation between different heights with distance in the horizontal plane (not shown here).

Both techniques demonstrate that the spatial characteristics of coherent boundary-layer structures are affected by the ambient wind. With the cumulant-based technique, this manifests as an elongation across all scalar fields in the direction of shear. The object-based approach refines this insight by quantifying how individual structures are stretched planar and tilt in the direction of the ambient wind. A further benefit of the object-based approach over bulk length-scale estimates is the technique's ability to quantify the spatial characteristics of the individual objects that dominate the vertical flux. This enabled us to show the plume-like behaviour of vertical transport in the boundary layer and measure how these structures are affected by ambient conditions (e.g., shear in this case). To gain insight relevant to producing analytic models of boundary-layer transport, future work should utilise such an object-based approach.

# 6 | CONCLUSIONS AND FURTHER WORK

This article has demonstrated two methods by which to characterise the shape, size, and orientation of coherent structures. The first method quantifies the horizontal orientation and length-scale of coherence between any two

scalar fields, and through this makes it possible to measure the coherence in the boundary layer as a whole. The second method identifies cloud-feeding coherent structures using a decaying passive tracer and is able to quantify length-scales and orientation (both vertical and horizontal) for each of these objects, allowing for a more instructive decomposition where the nonlocal transport by individual coherent structures can be studied.

We have made use of cumulants to measure coherence length-scales and orientation for different scalar fields and fluxes of these fields in the bulk of the boundary layer. This showed that, in the absence of shear, vertical velocity features were significantly narrower ($\approx 200$ m) than the moisture and potential temperature fields ($\approx 1,000$ m), but of a similar scale to a surface-released passive tracer ($\approx 300$ m). This method is also able to quantify the elongation of spatial coherence and calculate the elongation direction, showing how the presence of ambient wind shear causes elongation (along with the wind direction in this case) of the vertical velocity field and a less pronounced change to the heat and moisture fields.

We additionally demonstrated that using a surface-released radioactive tracer tracks air with thermodynamic properties statistically similar to air entering through the cloud base of newly formed clouds. This allowed for the identification of individual cloud-feeding coherent structures. By decomposing the vertical flux by the vertical extent of each structure, it was found that the vertical flux is dominated by structures extending from the surface, through cloud base, and into cloud. This insight suggests that flux-dominating structures are more plume-like (carrying transport from the surface and throughout the boundary layer) rather than thermal-like. The parts of these structures carrying out transport in the boundary layer were then characterised using Minkowski functionals (producing a characteristic length, width, and thickness for each object) and a technique for calculating an object's tilt and horizontal orientation. With these methods, it was shown that, although the majority of coherent structures are closest to a sphere in shape, the structures that dominate the vertical flux in the boundary layer are generally thicker than they are wide (4:3 ratio); an asymmetry that increases in the presence of ambient shear (2:1) as the structures are stretched planar. In the absence of shear, the structures do generally exhibit some degree of tilt ($\theta \approx 10°$), but this has no particular orientation, whereas in the presence of shear objects were more tilted ($\theta \approx 40°$) and all in the direction of the ambient wind. These findings cannot be made through a bulk estimate of the length-scale of coherence, as was done in previous work, but require identification and measurement of individual coherent structures.

These findings suggest that, when formulating models to represent transport by cloud-feeding coherent boundary-layer structures, the most appropriate model may be a plume, at least for the kind of (shallow moist convective) boundary layer studied here. In the presence of shear, planar stretching and tilting (Bursik, 2001, possibly increasing the entrainment of dry air) of these structures may be necessary to consider when constructing a parametrisation of boundary-layer transport. Further study can explore the generality of this conclusion to other boundary-layer configurations, for example, land-based, heterogeneously forced, deep convective, etc. Similarly, the techniques presented herein may be used to study the relationship between the spatial characteristics of coherent boundary-layer structures and the spatial characteristics of the clouds they form.

## AUTHOR CONTRIBUTIONS

**Leif Denby:** conceptualization; data curation; formal analysis; investigation; methodology; project administration; visualization. **Steven J. Böing:** funding acquisition; project administration; resources. **Douglas J. Parker:** conceptualization; funding acquisition; project administration; supervision. **Andrew N. Ross:** conceptualization; funding acquisition; supervision. **Steven M. Tobias:** conceptualization; methodology; supervision.

## ORCID

*Leif Denby* https://orcid.org/0000-0002-7611-9222
*Steven J. Böing* https://orcid.org/0000-0003-3794-2563
*Douglas J. Parker* https://orcid.org/0000-0003-2335-8198
*Andrew N. Ross* https://orcid.org/0000-0002-8631-3512

## REFERENCES

Ait-Chaalal F., Schneider T., Meyer B. and Marston J. B. (2016) Cumulant expansions for atmospheric flows. *New Journal of Physics*, 18, (2), 025019. http://dx.doi.org/10.1088/1367-2630/18/2/025019

Berg, L.K. and Stull, R.B. (2004) Parameterization of joint frequency distributions of potential temperature and water vapor mixing ratio in the daytime convective boundary layer. *Journal of the Atmospheric Sciences*, 61, 813–828.

Bony, S., Stevens, B., Ament, F., Bigorre, S., Chazette, P., Crewell, S., Delanoë, J., Emanuel, K., Farrell, D., Flamant, C., Gross, S.,

Hirsch, L., Karstensen, J., Mayer, B., Nuijens, L., Ruppert, J.H., Sandu, I., Siebesma, P., Speich, S., Szczap, F., Totems, J., Vogel, R., Wendisch, M. and Wirth, M.(2017) EUREC4A: a field campaign to elucidate the couplings between clouds, convection and circulation. *Surveys in Geophysics*, 38, 1529–1568. http://link.springer.com/10.1007/s10712-017-9428-0.

Brient, F., Couvreux, F., Villefranque, N., Rio, C. and Honnert, R. (2019) Object-oriented identification of coherent structures in large eddy simulations: importance of downdrafts in stratocumulus. *Geophysical Research Letters*, 46, 2854–2864.

Brown, A.R. and Grant, A.L. (1997) Non-local mixing of momentum in the convective boundary layer. *Boundary-Layer Meteorology*, 84, 1–22.

Bursik, M. (2001) Effect of wind on the rise height of volcanic plumes. *Geophysical Research Letters*, 28, 3621–3624. https://doi.org/10.1029/2001GL013393/full.

Chinita, M.J., Matheou, G. and Teixeira, J. (2018) A joint probability density-based decomposition of turbulence in the atmospheric boundary layer. *Monthly Weather Review*, 146, 503–523.

Couvreux, F., Hourdin, F. and Rio, C. (2010) Resolved versus parametrized boundary-layer plumes. Part I: a parametrization-oriented conditional sampling in large-eddy simulations. *Boundary-Layer Meteorology*, 134, 441–458. http://link.springer.com/10.1007/s10546-009-9456-5.

Dawe, J.T. and Austin, P.H. (2012) Statistical analysis of an LES shallow cumulus cloud ensemble using a cloud tracking algorithm. *Atmospheric Chemistry and Physics*, 12, 1101–1119.

Deardorff, J.W. (1966) The counter-gradient heat flux in the lower atmosphere and in the laboratory. *Journal of the Atmospheric Sciences*, 23, 503–506. https://doi.org/10.1175/1520-0469%281966%29023%3C0503%3ATCGHFI%3E2.0.CO%3B2.

Denby, L. and Liberzon, A. (2020). GENESIS toolkit for analysing atmospheric coherent structures. https://doi.org/10.5281/zenodo.5805182.

de Roode, S.R., Duynkerke, P.G. and Jonker, H.J. (2004) Large-eddy simulation: how large is large enough? *Journal of the Atmospheric Sciences*, 61, 403–421.

Devenish, B.J., Rooney, G.G., Webster, H.N. and Thomson, D.J. (2010) The entrainment rate for buoyant plumes in a crossflow. *Boundary-Layer Meteorology*, 134, 411–439.

Efstathiou, G.A., Thuburn, J. and Beare, R.J. (2020) Diagnosing coherent structures in the convective boundary layer by optimizing their vertical turbulent scalar transfer. *Boundary-Layer Meteorology*, 174, 119–144. https://doi.org/10.1007/s10546-019-00480-1.

Etling, D. and Brown, R.A. (1993) Roll vortices in the planetary boundary layer: a review. *Boundary-Layer Meteorology*, 65, 215–248.

Grant, A.L.M. and Brown, A.R. (1999) A similarity hypothesis for shallow-cumulus transports. *Quarterly Journal of the Royal Meteorological Society*, 125, 1913–1936. https://doi.org/10.1002/qj.49712555802.

Heus, T. and Seifert, A. (2013) Automated tracking of shallow cumulus clouds in large domain, long duration large eddy simulations. *Geoscientific Model Development*, 6, 1261–1273.

Holtslag, A.A. and Nieuwstadt, F.T. (1986) Scaling the atmospheric boundary layer. *Boundary-Layer Meteorology*, 36, 201–209.

Holtslag, A.A.M.and Moeng, C.-H. (1991) Eddy diffusivity and countergradient transport in the convective atmospheric boundary layer. *Journal of the Atmospheric Sciences*, 48, 1690–1698.

https://journals.ametsoc.org/jas/article/48/14/1690/22553/Eddy-Diffusivity-and-Countergradient-Transport-in.

Houze, R.A. (2014) *Cloud Dynamics*. Academic Press. https://books.google.co.uk/books?id=spYRAQAAIAAJ.

Jones E, Oliphant, T., Peterson, P. et al. (2020) SciPy 1.0: fundamental algorithms for scientific computing in Python. Nature Methods, 17, (3), 261–272. http://dx.doi.org/10.1038/s41592-019-0686-2.

Jonker, H.J.J., Duynkerke, P.G. and Cuijpers, J.W.M. (1999) Mesoscale fluctuations in scalars generated by boundary layer convection. *Journal of the Atmospheric Sciences*, 56, 801–808. https://doi.org/10.1175/1520-0469%281999%29056%3C0801%3AMFISGB%3E2.0.CO%3B2.

Khanna, S. and Brasseur, J.G. (1998) Three-dimensional buoyancy- and shear-induced local structure of the atmospheric boundary layer. *Journal of the Atmospheric Sciences*, 55, 710–743.

Lauritzen, S.L. (2002) *Thiele: Pioneer in Statistics*. Oxford: Oxford University Press. http://www.oxfordscholarship.com/oso/public/content/maths/9780198509721/toc.html.

Lenschow, D.H. and Sun, J. (2007) The spectral composition of fluxes and variances over land and sea out to the mesoscale. *Boundary-Layer Meteorology*, 125, 63–84.

Lohou, F., Druilhet, A., Campistron, B., Redelspergers, J.L. and Saïd, F. (2000) Numerical study of the impact of coherent structures on vertical transfers in the atmospheric boundary layer. *Boundary-Layer Meteorology*, 97, 361–383.

Mecke, K.R. (2000) Additivity, convexity, and beyond: Applications of Minkowski functionals in statistical physics. In: *Statistical Physics and Spatial Statistics*, pp. 111–184. Berlin: Springer. http://link.springer.com/10.1007/3-540-45043-2_6.

Miao, Q., Geerts, B. and LeMone, M. (2006) Vertical velocity and buoyancy characteristics of coherent echo plumes in the convective boundary layer, detected by a profiling airborne radar. *Journal of Applied Meteorology and Climatology*, 45, 838–855.

Minkowski, H. (1903) Volumen und Oberfläche. *Mathematische Annalen*, 57, 447–495. URL http://link.springer.com/10.1007/978-3-322-90190-3_7 http://link.springer.com/10.1007/BF01445180.

Neggers R.A.J., Köhler M. and Beljaars A.C.M. (2009) A Dual Mass Flux Framework for Boundary Layer Convection. Part I: Transport. *Journal of the Atmospheric Sciences*, 66, (6), 1465–1487. http://dx.doi.org/10.1175/2008jas2635.1

Neggers, R.A. (2009b) A dual mass flux framework for boundary layer convection. Part II: Clouds. *Journal of the Atmospheric Sciences*, 66, 1489–1506.

Nicholls, S. and Lemone, M.A. (1980) The fair weather boundary layer in GATE: the relationship of subcloud fluxes and structure to the distribution and enhancement of cumulus clouds. *Journal of the Atmospheric Sciences*, 37, 2051–2067.

Park, S.B., Böing, S. and Gentine, P. (2018) Role of surface friction on shallow nonprecipitating convection. *Journal of the Atmospheric Sciences*, 75, 163–178.

Park, S.B., Gentine, P., Schneider, K. and Farge, M. (2016) Coherent structures in the boundary and cloud layers: role of updrafts, subsiding shells, and environmental subsidence. *Journal of the Atmospheric Sciences*, 73, 1789–1814.

Poelaert, D., Schniewind, J. & Janssens, F. (2011). Surface area and curvature of the general ellipsoid. http://arxiv.org/abs/1104.5145.

Rauber, R.M., Ochs, H.T., Di Girolamo, L., Göke, S., Snodgrass, E., Stevens, B., Knight, C., Jensen, J.B., Lenschow, D.H., Rilling, R.A., Rogers, D.C., Stith, J.L., Albrecht, B.A., Zuidema, P., Blyth, A.M., Fairall, C.W., Brewer, W.A., Tucker, S., Lasher-Trapp, S.G., Mayol-Bracero, O.L., Vali, G., Geerts, B., Anderson, J.R., Baker, B.A., Lawson, R.P., Bandy, A.R., Thornton, D.C., Burnet, E., Brenguier, J.-L., Gomes, L., Brown, P.R.A., Chuang, P., Cotton, W.R., Gerber, H., Heikes, B.G., Hudson, J.G., Kollias, P., Krueger, S.K., Nuijens, L., O'Sullivan, D.W., Siebesma, A.P. and Twohy, C.H. (2007) Rain in shallow cumulus over the ocean: the RICO campaign. *Bulletin of the American Meteorological Society*, 88, 1912–1928. http://journals.ametsoc.org/doi/abs/10.1175/BAMS-88-12-1912.

Rio, C. and Hourdin, F. (2008) A thermal plume model for the convective boundary layer: representation of cumulus clouds. *Journal of the Atmospheric Sciences*, 65, 407–425.

Rio, C., Hourdin, F., Couvreux, F. and Jam, A. (2010) Resolved versus parametrized boundary-layer plumes. Part II: continuous formulations of mixing rates for mass-flux schemes. *Boundary-Layer Meteorology*, 135, 469–483.

Sahni, V., Sathyaprakash, B.S. and Shandarin, S.F. (1998) Shapefinders: a new shape diagnostic for large-scale structure. *The Astrophysical Journal*, 495, L5–L8.

Salesky, S.T., Chamecki, M. and Bou-Zeid, E. (2017) On the nature of the transition between roll and cellular organization in the convective boundary layer. *Boundary-Layer Meteorology*, 163, 41–68.

Schmalzing, J. and Buchert, T. (1997) Beyond genus statistics: a unifying approach to the morphology of cosmic structure. *The Astrophysical Journal*, 482, L1–L4.

Schmalzing, J., Buchert, T., Melott, A.L., Sahni, V., Sathyaprakash, B.S. and Shandarin, S.F. (1999) Disentangling the cosmic web. I. Morphology of isodensity contours. *The Astrophysical Journal*, 526, 568–578.

Schmidt, H. and Schumann, U. (1989) Coherent structure of the convective boundary layer derived from large-eddy simulations. *Journal of Fluid Mechanics*, 200, 511–562.

Schumann, U. and Moeng, C.-H. (1991) Plume fluxes in clear and cloudy convective boundary layers. *Journal of the Atmospheric Sciences*, 48, 1746–1757. https://journals.ametsoc.org/jas/article/48/15/1746/22406/Plume-Fluxes-in-Clear-and-Cloudy-Convective.

Seifert, A., Heus, T., Pincus, R. and Stevens, B. (2015) Large-eddy simulation of the transient and near-equilibrium behavior of precipitating shallow convection. *Journal of Advances in Modeling Earth Systems*, 7, 1918–1937. https://doi.org/10.1002/2015MS000489.

Siebesma, A.P., Bretherton, C.S., Brown, A., Chlond, A., Cuxart, J., Duynkerke, P.G., Jiang, H., Khairoutdinov, M., Lewellen, D., Moeng, C.-H., Sanchez, E., Stevens, B. and Stevens, D.E. (2003) A large eddy simulation intercomparison study of shallow cumulus convection. *Journal of the Atmospheric Sciences*, 60, 1201–1219. https://journals.ametsoc.org/jas/article/60/10/1201/103861/A-Large-Eddy-Simulation-Intercomparison-Study-of.

Siebesma, A.P., Soares, P.M.M. and Teixeira, J. (2007) A combined eddy-diffusivity mass-flux approach for the convective boundary layer. *Journal of the Atmospheric Sciences*, 64, 1230–1248.

Stevens, B., Moeng, C.-H., Ackerman, A.S., Bretherton, C.S., Chlond, A., de Roode, S., Edwards, J., Golaz, J.-C., Jiang, H., Khairoutdinov, M., Kirkpatrick, M.P., Lewellen, D.C., Lock, A., Müller, F., Stevens, D.E., Whelan, E. and Zhu, P. (2005) Evaluation of large-eddy simulations via observations of nocturnal marine stratocumulus. *Monthly Weather Review*, 133, 1443–1462.

Stevens, B. and Seifert, A. (2008) Understanding macrophysical outcomes of microphysical choices in simulations of shallow

cumulus convection. *Journal of the Meteorological Society of Japan*, 86A, 143–162.

Stull, R.B. (1985) A fair-weather cumulus cloud classification scheme for mixed-layer studies. *Journal of Climate and Applied Meteorology*, 24, 49–56. http://journals.ametsoc.org/doi/10.1175/1520-0450(1985)024%3C0049:AFWCCC%3E2.0.CO;2.

Tobias, S.M. and Marston, J.B. (2017) Three-dimensional rotating Couette flow via the generalised quasilinear approximation. *Journal of Fluid Mechanics*, 810, 412–428. https://www.cambridge.org/core/product/identifier/S0022112016007278/type/journal_article.

VanZanten, M.C., Stevens, B., Nuijens, L., Siebesma, A.P., Ackerman, A.S., Burnet, F., Cheng, A., Couvreux, F., Jiang, H., Khairoutdinov, M., Kogan, Y., Lewellen, D.C., Mechem, D., Nakamura, K., Noda, A., Shipway, B.J., Slawinska, J., Wang, S. and Wyszogrodzki, A. (2011) Controls on precipitation and cloudiness in simulations of trade-wind cumulus as observed during RICO. *Journal of Advances in Modeling Earth Systems*, 3.

Young, G.S., Kristovich, D.A.R., Hjelmfelt, M.R. and Foster, R.C. (2002) Supplement to rolls, streets, waves, and more. *Bulletin of the American Meteorological Society*, 83, 1001–1001. https://doi.org/10.1175/BAMS-83-7-Young.

Zhdankin V., Boldyrev S., Perez J.C. and Tobias S.M. (2014) Energy dissipation in magnetohydrodynamic turbulence: coherent structures or "nanoflares"?. *The Astrophysical Journal*, 795, (2), 127. http://dx.doi.org/10.1088/0004-637x/795/2/127

## APPENDIX A. TIME-SCALE OF CONVECTIVE OVERTURNING IN BOUNDARY LAYER

Using the subcloud characteristic velocity scale $w_*$ (as in Holtslag and Nieuwstadt, 1986, but corrected for the contribution to buoyancy from water vapour) and the boundary-layer depth $z_{BL}$, we can calculate a subcloud convective overturning time-scale $\tau_{BL}$ as

$$\tau_{BL} = \frac{z_{BL}}{w_*}. \tag{A1}$$

The subcloud convective velocity scale is given as

$$w_* = \left( \overline{w'b'}\Big|_0 z_{BL} \right)^{1/3}, \tag{A2}$$

with buoyancy flux

$$\overline{w'b'}\Big|_0 = \frac{g}{T_{v,0}} \overline{w'\theta'_v}\Big|_0, \tag{A3}$$

and virtual potential temperature flux (approximately) given by (de Roode *et al.*, 2004)

$$\overline{w'\theta'_v}\Big|_0 = \overline{w'\theta'}\Big|_0 + \frac{R_v}{R_d}\overline{\theta}_0 \overline{w'q'}\Big|_0, \tag{A4}$$

where $z_{BL}$ is the boundary-layer depth, $g$ the gravitational acceleration, and $|_0$ denotes surface values. With surface fluxes for sensible $\overline{w'\theta'}\Big|_0 = F_s/(\rho_0 c_{p,d})$ and latent heat $\overline{\theta}_0 \overline{w'q'}\Big|_0 = F_v/(\rho_0 L_v)$, surface moisture $q_{v,0} = 15\ \mathrm{g \cdot kg^{-1}}$, surface temperature $T_0 = 300\ \mathrm{K}$, and diagnosed boundary-layer depth $z_{BL} = 650\ \mathrm{m}$ (here taken as the cloud-base height), the convective overturning time-scale becomes $\tau_{BL} = 16\ \mathrm{min}$. The constants used above are those for density of dry air $\rho_0 = 1.2\ \mathrm{kg^3 \cdot m^{-1}}$, latent heat of vaporisation $L_v = 2.5 \times 10^6\ \mathrm{J \cdot kg^{-1}}$, specific heat capacity of dry air $c_{p,d} = 1,005\ \mathrm{J \cdot kg^{-1} \cdot K^{-1}}$, and gas constants for dry air $R_d = 287\ \mathrm{J \cdot kg^{-1} \cdot K^{-1}}$ and water vapour $R_v = 461\ \mathrm{J \cdot kg^{-1} \cdot K^{-1}}$.

## APPENDIX B. CROFTON'S FORMULA FOR DISCRETE INTEGRALS

Evaluating the integrals of the Minkowski functionals numerically in 3D (Equations 5–8) is nontrivial on discrete 3D masks, as these structures are necessarily blocky and so construction of, for example, the surface normal at a corner is poorly defined.

Instead of approximating the surface normals, the integral in the Minkowski functionals can be approximated discretely using Crofton's formula (Schmalzing *et al.*, 1999). This amounts to counting the number of vertices ($N_0$), edges ($N_1$), faces ($N_2$), and cells ($N_3$) on both the interior and exterior of the cubical voxels contained in a given object mask. With these, the Minkowski functionals in 3D are given as

$$V_0 = N_3, \qquad V_1 = 2\frac{N_2 - 3N_3}{9\Delta x},$$

$$V_2 = 2\frac{N_1 - 2N_2 + 3N_3}{9\Delta x^2}, \qquad V_3 = \frac{N_0 - N_1 + N_2 - N_3}{\Delta x^3}.$$

It can be shown, for shapes where analytical forms for the Minkowski functionals exist, that these approximate definitions converge to the true values when $\Delta x \to \infty$. Note that the above approximations assume the underlying grid to have isotropic grid spacing ($\Delta x = \Delta y = \Delta z$).

# APPENDIX C. CALCULATION OF SLOPE AND ORIENTATION OF INDIVIDUAL OBJECTS

The $xy$-orientation angle ($\phi$ measured from the $x$-axis) and tilt angle $\theta$ (measured from the $z$-axis) are calculated from characteristic slope scales $\overline{\Delta x}, \overline{\Delta y}, \overline{\Delta z}$:

$$\phi = \arctan 2(\overline{\Delta y}, \overline{\Delta x}), \qquad \theta = \arctan 2(\overline{\Delta l_{xy}}, \overline{\Delta z}),$$

$$\Delta l_{xy} = \sqrt{\overline{\Delta x}^2 + \overline{\Delta y}^2},$$

which are evaluated as area-weighted changes in the centroid position:

$$\overline{\Delta x} = \frac{\Delta z}{V} \sum_k A(z_k) \frac{x^c(z_{k+1}) - x^c(z_{k-1})}{2},$$

$$\overline{\Delta y} = \frac{\Delta z}{V} \sum_k A(z_k) \frac{y^c(z_{k+1}) - y^c(z_{k-1})}{2},$$

$$\overline{\Delta z} = \frac{\Delta z}{V} \sum_k A(z_k) \frac{z^c(z_{k+1}) - z^c(z_{k-1})}{2},$$

where $x_c(k)$, $y_c(k)$, and $A(k)$ are the centroid's $x$ and $y$ position, and area at height index $k$, respectively, and $V$ the volume, given by

$$A(z_k) = \sum_{i,j} m(x_i, y_j, z_k) \Delta x \Delta y, \quad V = \sum_{i,j,k} m(x_i, y_j, z_k) \Delta x \Delta y \Delta z,$$

$$x^c(z_k) = \frac{\sum_{i,j} x_i \, m(x_i, y_j, z_k)}{\sum_{i,j} m(x_i, y_j, z_k)}, \quad y^c(z_k) = \frac{\sum_{i,j} y_i \, m(x_i, y_j, z_k)}{\sum_{i,j} m(x_i, y_j, z_k)},$$

for an individual object defined by the mask $m$ and grid spacing $\Delta x, \Delta y, \Delta z$.